UNIVERSITÀ DEGLI STUDI DI TRIESTE

Sede Amministrativa del Dottorato di Ricerca

DOTTORATO DI RICERCA IN GEOFISICA APPLICATA E IDRAULICA
XIX CICLO

AN INVESTIGATION OF PARTICLE DISPERSION IN A TIDALLY DRIVEN TURBULENT FLOW

(Settore scientifico-disciplinare ICAR 01)

Dottorando: GUIDO LUPIERI

Coordinatore del Collegio Docenti: Prof. Rinaldo Nicolich
Università degli Studi di Trieste

Tutore e Relatore: Prof. Vincenzo Armenio
Università degli Studi di Trieste

UNIVERSITÀ DEGLI STUDI DI TRIESTE

Sede Amministrativa del Dottorato di Ricerca

DOTTORATO DI RICERCA IN GEOFISICA APPLICATA E IDRAULICA
XIX CICLO

An investigation of particle dispersion in a tidally driven turbulent flow

(Settore scientifico-disciplinare ICAR 01)

Dottorando: Guido Lupieri

Coordinatore del Collegio Docenti: Prof. Rinaldo Nicolich
Università degli Studi di Trieste

Tutore e Relatore: Prof. Vincenzo Armenio
Università degli Studi di Trieste

Contents

Chapter 1

Introduction

1.1 An overview on the problem of particle dispersion in the Gulf of Trieste

The analysis of the hydrodynamic characteristics of a dispersed phase in a shallow water basin is a relevant task for the understanding of the processes that typically occur in coastal applications, from pollutant dispersion to biological feeding mechanisms.
In a coastal basin, the advective transport is mainly driven by the horizontal components of the velocity field and depends upon the characteristics of the coastline. In spite of it, vertical mixing is usually governed by the three dimensional turbulent regime that develops in the water column. In particular, the following features rule the vertical mixing in coastal applications: the shallowness of the water column, the turbulence generated at the bottom boundary layer by a current that drives the flow, the turbulent mixing at the free-surface region supplied by wind stress and wave breaking, the Earth rotation and at last, also the presence of thermal and/or haline stratification can play an important role. These features will be shortly discussed in the next section.

The Gulf of Trieste, subset of our investigation, is a shallow water inlet with a mean depth of 17 m (maximum 25 m) and an area of about 20 km $\times$ 25 km. It is located in the north area of the Adriatic Sea. Fig.1.1 shows the location of the Gulf of Trieste in the Mediterranean Sea.

The dynamics of the Gulf is characterized by seasonal variability of temperature and density, and the mixing and dispersion processes are strongly dependent to this context. This variability is due to the combined effects of many factors such as the presence of a strong wind (Bora) whose action is directly related to the water column instability, the input of fresh water from the river Isonzo and the water exchange due to Adriatic sea currents. For all this phenomena an extended quantity of measured data have been collected from more than one hundred years: the interest in the knowledge

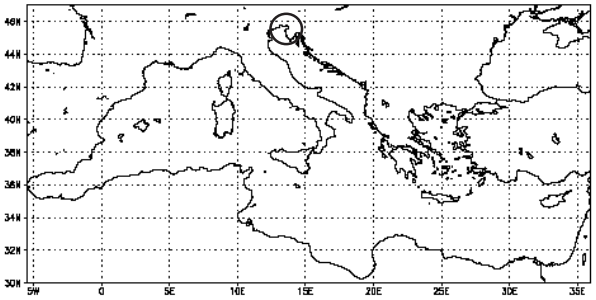

Figure 1.1: In the Figure is represented the Mediterranean Sea and in the small circle the Gulf of Trieste location.

of these processes is due to the deep impact in the local economy (from fishing to tourism). This allows a correct formulation of the forcing acting in the dispersion problem regarding the Gulf.

1.2 The relevant features concurring in the dispersion and the mixing processes in the Gulf of Trieste

Here we analyze the most important effects governing the dispersion and the mixing processes in a shallow water column located in the Trieste Gulf.

In the Gulf of Trieste, the horizontal fluid velocity field is subjected to the combination of the tidal motion and inertial currents. Even if they have small intensity, the inertial currents represent an efficient mechanism in the water exchange between the Adriatic Sea and the Gulf. In general, the horizontal component of sea currents velocity decreases in amplitude with the depth of the basin and spans a range of values from 40 cm/s to 5 cm/s usually present in the middle of the Gulf [1].
A typical scenario occurring in the Gulf includes sea breezes affecting the top of the water column, while the bottom is subjected to anticlockwise currents coming from the South.

Tidal upwards generate a boundary layer extending from the bottom water column up and assume the typical character of an oscillating flow with zero mean velocity along one complete period of oscillation. When the same period of oscillation is considered and due to the combination between tide and the Coriolis force, the trajectory of a drifter results elliptic. For this reason, tides are not directly involved in the interchange of water between the Gulf and the Adriatic Sea. The effect of tide is to produce an excursion of free surface level. This happens almost simultaneously in all the Gulf because of the relatively high propagation speed of tide, proportional to the

depth of the basin, while it takes a delay of one hour to reach the Grado Lagoon (located in the North-West with respect to the Gulf position), where the basin depth is smaller.
The major constituent and measured tidal components acting in the basin considered are seven: $M_2, S_2, N_2, K_2, K_1, O_1$ and P_1. They are commonly used in tidal prediction by means of the classical harmonic method [2] in which tidal oscillation is considered as the sum of harmonic components. One is the fundamental (the M2 semidiurnal component), responsible of the maximum excursion of free surface level, and here considered as the mainforcing of our numerical simulation.

component	M2	S2	N2	K2	K1	O1	P1
period (hrs)	12.42	12.00	12.65	11.96	23.93	25.81	24.06
amplitude (cm)	26.7	16.0	4.5	4.3	18.2	5.4	6.0

Table 1.1: In the table are showed the tidal harmonic constant for the Gulf of Trieste: the period of oscillation expressed in hours and the amplitude expressed in cm.

The main direction of the tidal current can be considered perpendicular to the Eastern coast if we are far from the coast, while very close to the coast the current is directed along-shore.
In a shallow water environment the circulation near the coast can depend on local features (bathymetry, temperature gradients and wind), and secondary currents can be induced. Since we are interested in simulating an archetype of a shallow water environment, we consider our numerical experiment as located far from the coast. The frame of reference will be aligned with the $x-$ axis directed from SW to NE (as reported in Fig.1.2), rotated of an angle $\gamma = 45°$ with respect to the North.

Phenomena due to wind, such as the wavebreaking and (when induced) the Langmuir circulation can play a relevant role in the dynamic of the air-sea interface. In the first case, the turbulence at the air-sea interface results increased and the energy profiles do not to follow precisely the log of the wall [3]: the complete energy budget at sea surface has to include an extra dissipation term due to the break of wave fronts [4]. Due to the combined effects of the wind speed and the Stokes drift velocity, the importance of the Langmuir circulation is related to the vertical fluid velocity induced in the rotating characteristic structures: it is comparable to that of upwelling and downwelling processes and therefore relevant in the surface mixing processes. As an example, air bubbles are transported from the surface and therefore oxygen mixing results enhanced; furthermore, Langmuir cells are capable to break the surface stratification barrier ensuring vertical mixing processes [5].

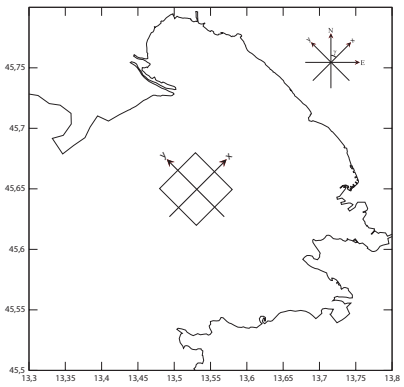

Figure 1.2: A sketch of the domain location: in the $x-$ direction it is aligned with the driving tidal flow, the rotation angle with respect to North is $\gamma = 45°$. The $z-$ axis is normal to the paper pointing toward the reader.

In Fig.1.3 we show a representation of the annual distribution of wind preferential direction. The mean is taken in a range of 10 years $(1991 - 2000)$ and Bora (from NE) results as the most present on the Gulf [6].

In the Gulf of Trieste, the stratification of the fluid column shows a strong seasonal variation: during the winter the water column has an homogeneous vertical distribution of temperature and during the summer a stable stratification profile is present, with water density increasing with depth. This is showed in Fig.1.4, where are reported two vertical temperature profiles measured in February and July (further details can be found on [7]). Under the case of a strong stable stratification, as that in the July case, a potential barrier tends to suppress the vertical mixing and the presence of internal waves [8], [9].
In this case, another characteristic scenario involves the role of the wind: the summer surface heating can create the strong stratification that inhibits the vertical mixing of the fluid column, while the action of the Bora wind has the effect of destabilize the column density profile by transferring energy and cooling the sea surface directly, inducing indirectly also the upwelling of deep water.
During the winter, this mechanism is reduced. In our numerical experiment, we are interested in the winter case when a neutral stratification condition is present.

The turbulence in the water column is originated by the presence of the bottom boundary layer and propagates inducing 3-D mixing processes that are crucial for life (for example in the transport of micro-organisms) as much as determinant for the dispersion of pollutant agents. The presence of

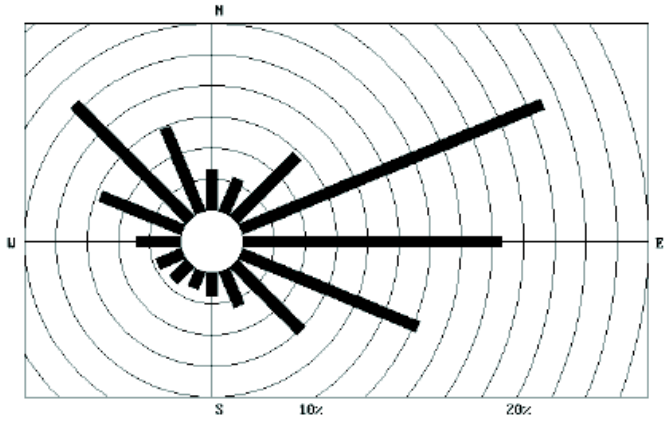

Figure 1.3: Annual distribution in percentage on wind preferential direction.

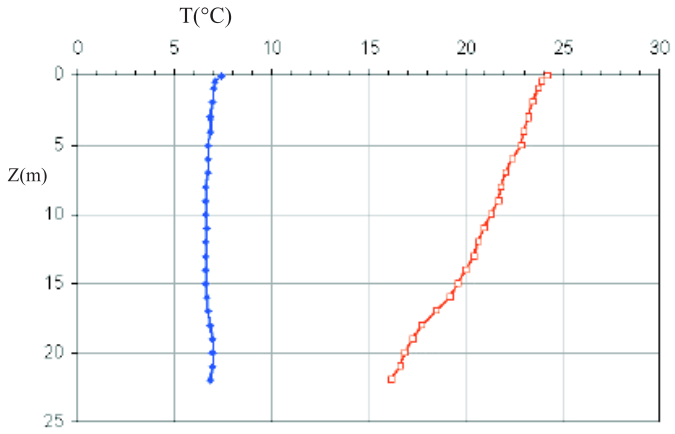

Figure 1.4: Typical vertical profiles of temperature measured in the Gulf of Trieste in February (left) and July (right).

a turbulent regime in the shallow water column will be considered in terms of the Reynolds number of the flux and discussed in Sec.1.3.

The Coriolis parameter at mid-latitude is $f = 2\Omega sin\phi \simeq 10^{-4}$ rad/s, where $\Omega = 7.272 \times 10^{-5}$ rad/s is the magnitude of the angular velocity of Earth and $\phi = 45^{\circ}$ is the latitude. This is also the case of the Gulf of Trieste where this value corresponds to a period $T_f = 2\pi/f \simeq 17.4$ hours. According to Fig.1.2 we properly decompose the angular velocity in the following components:

$$\Omega_i = (\Omega_x, \Omega_y, \Omega_z) = \Omega(1/2, 1/2, 1/\sqrt{2}) = f(1/2\sqrt{2}, 1/2\sqrt{2}, 1/2).$$

Such forcing gives rise to a bottom Ekman layer that interacts with the oscillating boundary layer due to inertial currents and tides. In absence of a wind stress at the free surface, the upper Ekman layer does not develop.

1.3 The governing parameters in the considered case

We study the case of particle dispersion in an oscillating flow driven by the main tidal component and subjected to the Coriolis force in neutral stratification conditions.
In order to do that, we can derive the large scale Reynolds number, related to the estimated maximum bulk velocity U_0 (hereafter with the term *bulk* we denote a quantity averaged in space along a cross-sectional area at a given time instant, whereas the term *maximum* refers to the maximum value that the bulk quantity gets along the period of oscillation), the height of the water column h and the viscosity of the water $\nu = 1.15 \times 10^{-6}$ m^2/s.
A value of $h = 16$ m will be considered in our numerical experiment as measured at 500 m from the coast where a buoy is placed: MAMBO buoy, from Istituto Nazionale di Oceanografia e Geofisica Sperimentale (OGS) is precisely located at $45^{\circ}41.54'N, 13^{\circ}42.30'E$. Consistently with Malačič [10], we assume a value of $U_0 = 0.05$ m/s for the maximum inertial velocity induced by the pressure gradient driving the flow, and we obtain the outer Reynolds number of $Re_h = 0.7 \times 10^6$. The harmonic pressure gradient is assumed aligned in the $x-$ direction:

$$\frac{dP(t)}{dx} = -U_0 \omega_{M2} cos(\omega_{M2} t) \tag{1.1}$$

with $\omega_{M2} = 2\pi f_{M2} = 1.4 \times 10^{-4}$ rad/s the angular frequency of tidal oscillation. The time dependent pressure gradient defined above results into the following oscillating bulk velocity:

$$U(t) = U_0 sin(\omega_{M2} t) \tag{1.2}$$

with the estimated amplitude of motion $a = U_0/\omega_{M2} = 357$ m. It means that in a period of oscillation, a drifter set in a rotating frame of reference and driven by the $M2$ tide, follows an harmonic path whose amplitude is about 700 m long.
We can also define the inertial Re number depending upon the amplitude of the motion a and related to the oscillating flow as $Re_{M2} = aU_0/\nu = 15\times10^6$. In oscillating flows, a Reynolds number based on the thickness of the laminar Stokes boundary layer is commonly defined. In our case, the laminar Stokes BL is $\delta_S = \sqrt{2\nu/\omega_{M2}} \simeq 0.13$m, that gives $Re_S = \delta_S U_0/\nu \simeq 5600$.

Another important parameter we refer to is the Keulegan-Carpenter number KC, that is the ratio between the oscillation period $T_{M2} = 1/f_{M2}$ and the inertial time scale h/U_0; it reads as: $KC = U_0 T_{M2}/h = 2\pi a/h = 140$.

In our case, it is convenient to define the Rossby number as the ratio $Ro = \omega_{M2}/f = O(1)$ showing that the Coriolis force in this numerical experiment gives a contribute to the dynamic of the fluid of the same order of the tidal oscillation frequency.
We can rearrange the ratio between Reynolds numbers

$$\frac{Re_S}{Re_E} = \frac{1}{\sqrt{Ro}} \tag{1.3}$$

defined with the thickness of the Stokes boundary layer and the thickness of the boundary layer due to rotation of the frame of reference $\delta_E = \sqrt{2\nu/f}$. Increasing the values of Ro, the penetrating length tends to increase with respect to the Stokes length scale δ_S. In our case, a value of $Re_{\delta_E} = 2090$ gives $Ro = 1.36$.

Chapter 2

The problem formulation

2.1 The Eulerian-Lagrangian approach

The evaluation of the hydrodynamic characteristics of particle laden flows is a relevant task especially in practical applications, ranging from pollutant dispersion to biological feeding mechanisms. In general, the matter can be described as the motion of very small particles (a definition will be further provided) which can deform (as in the case of air bubbles in water) or not under the action of a fluid dynamic field. The complexity of the physical problem is generally due the characteristics of the particles (such as size, shape and density) and of the moving fluid: the density of the particles can be comparable to that of the fluid or several times larger, particles with different size and shape are differently affected by the forces of the surrounding fluid, the same fluid is usually in a turbulent regime and the correct representation of the instantaneous motion is a relevant task in itself.

There are essentially two numerical approaches to deal with this problem: the Eulerian-Eulerian and the Eulerian-Lagrangian, where the first term is referred to the continuous phase and the second to the dispersed one.

In the Eulerian-Eulerian approach the concentration of the dispersed phase is usually defined and treated in a stochastic way by a diffusion constant that must be modeled. This decreases the computational cost of the simulation but it is hard to find suited models to each problem.

In the Eulerian-Lagrangian approach each particle is followed in the flow field. In this case three are the necessary elements: the fluid velocity field, the particle velocity field and the interpolator connecting them. The fluid is known just in the computational grid nodes and particles can step on different positions, therefore an interpolation is needed to provide the continuous phase velocity field at particle position. These elements, concurring on the solution of the Lagrangian tracking problem, are schematically represented in Fig.2.1.

In this approach, an accurate prediction of the flow field is requested as much as a correct representation of the forces acting over the particles in relative motion with the fluid. In comparison with the previous one, the computational cost (expressed in terms of both memory storage and CPU time) and the accuracy of the solution increase.

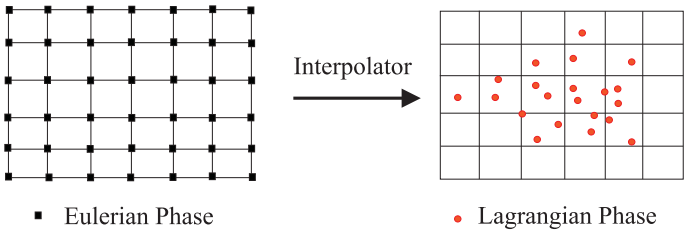

Figure 2.1: The three elements present in the Eulerian-Lagrangian frame for a particle dispersion problem are showed: squares on the left are the grid points and circles on the right represent particles; the connection is provided by the interpolation.

Being interested in the second approach, the continuous phase can be essentially resolved with three numerical techniques: the Direct Numerical Simulation (DNS), the Large Eddy Simulation (LES) and the Reynolds-Averaged Navier-Stokes (RANS).
In the DNS simulation, the Navier-Stokes equations of the fluid are completely resolved up to the dissipative scales and no modeling is developed. The computational amount grows with the grid number of points and the number of Reynolds [11].
In the RANS approach, the Navier-Stokes equations are averaged, usually assuming that the flux is in a steady state. A turbulence model turns out the scales of motion. In this case the computational grid can be coarser than that used in DNS and LES for the simulation of the same flux.
A compromise between accuracy in the results and computational requests is LES, where only the smallest scales are modeled. The choice of the eddy size to be resolved is left to a opportune filter. In Sec.3.1 the fundamental features of this technique are described.

The forces acting on particles are described by Maxey and Riley equations [12]. In this case a requested quantity is the fluid velocity field at particle position, to be provided by the interpolation. The choice of the interpolation scheme is done by a compromise between the accuracy and the computational cost: in our simulations, an interpolator based on Taylor series expansion, whose accuracy can be easily adapted to that of Navier-Stokes solver for the Eulerian phase, will be used.

2.2 The equations governing the continuous phase

We investigate the motion of fluid particles in a oscillating flow driven by the harmonic pressure gradient aligned in the streamwise direction as defined in Eq.1.1, and the same flow in a rotating frame of reference. In both cases, we consider the conditions of neutral stratification (winter case).

In this section will be given the details on the equations governing the continuous phase we intend to describe according the Eulerian-Lagrangian frame.

The equations governing the oscillating boundary layer in a rotating frame of reference in absence of vertical stratification are the incompressible Navier-Stokes equations of transport, written here in a dimensional form according Einstein notation:

$$\frac{\partial u_i}{\partial x_i} = 0 \tag{2.1}$$

$$\frac{\partial u_i}{\partial t} + \frac{\partial u_j u_i}{\partial x_j} = -\frac{1}{\rho_0}\frac{\partial p}{\partial x_i} + \nu\frac{\partial}{\partial x_j}\frac{\partial u_i}{\partial x_j} + F_1 + F_2 \tag{2.2}$$

where the frame of reference is expressed with the coordinates x_i; hereafter x_1, x_2, x_3 or x, y, z are used interchangeably for the the streamwise, the spanwise and the and wall-normal direction respectively. The velocity field is $u_i = (u, v, w)$, p the pressure and ρ_0 the reference density. The forcing F_1 and F_2 are respectively:

- $F_1 = -\frac{1}{\rho_0}\frac{dP(t)}{dx} = \frac{dU_i}{dt}$ due to the tidal current;
- $F_2 = 2\epsilon_{ijk}\Omega_j(U_k - u_k)$ due to Earth rotation; ϵ_{ijk} is Levi-Civita symbol.

The velocity $U_i = (U(t), 0, 0)$ represents the tidal current of Eq.1.2.
When the boundary and initial conditions are fixed, the motion of a fluid column is described by Eq.2.1 and Eq.2.2.

A non-dimensional form of the governing equations can be derived by using the reference parameters of Sec.1.3: the amplitude of motion $a = U_0/\omega_{M2}$ as the length scale, U_0 as the velocity scale and $a/U_0 = 1/\omega_{M2}$ as the time scale. Pressure is made non dimensional with $\rho_0 U_0^2$. In this case, Eq.2.1 and Eq.2.2 read:

$$\frac{\partial u_i}{\partial x_i} = 0 \tag{2.3}$$

$$\frac{\partial u_i}{\partial t} + \frac{\partial u_j u_i}{\partial x_j} = -\frac{\partial p}{\partial x_i} + \frac{1}{Re}\frac{\partial}{\partial x_j}\frac{\partial u_i}{\partial x_j} +$$

$$cos(t)\delta_{i1} + \frac{1}{Rosin(\phi)}\epsilon_{ijk}\epsilon_j(sin(t)\delta_{k1} - u_k) \tag{2.4}$$

2.3 The equations governing the Lagrangian phase

The Lagrangian approach of the dispersed phase provides to follow each particle as accelerated by the flow forces acting in its position. We are interested in the motion of fluid particles considered as a dispersed phase moving in the flow field described by Eq.2.1 and Eq.2.2. As discussed in Sec.2.1, we need a sufficiently accurate prediction of the Eulerian phase as much as a correct representation of the forces acting over each particle in relative motion with the fluid [13].

The general mathematical formulation of the forces acting on particles moving in a fluid is due to Maxey and Riley and requests several hypotheses:

- particles has the shape of a rigid sphere whose dimension is smaller than Kolmogorov scale
- particle Reynolds number is $Re_p = |u-v|a/\nu << 1$, with v the particle velocity, u the fluid velocity, a the particle radius and ν the cinematic viscosity
- the shear of the velocity field over the particle is very small, so there is not a lift due to the same vertical fluid velocity variations
- no contribution on fluid motion is due to particle-fluid interaction or particle-particle interaction. This is the one way coupling hypothesis, acceptable especially when a non-dense solution is taken into account and interactions among particles are extremely rare events.

The Maxey and Riley equations are provided here in the dimensional form:

$$\frac{dx_{p,i}}{dt} = v_i \tag{2.5}$$

and

$$m_p \frac{dv_i}{dt} = (m_p - m_f)g_i + m_f \frac{Du_i}{Dt} + 2\epsilon_{ijk} m_p u_{pj} \Omega_k -$$
$$\frac{1}{2} m_f [\frac{dv_i}{dt} - \frac{du_i}{dt} - \frac{1}{10} a^2 \frac{d(\nabla^2 u_i)}{dt}] - 6\pi a \mu (v_i - u_i - \frac{1}{6} a^2 \nabla^2 u_i) -$$
$$6\pi a^2 \mu \int_0^t d\tau \frac{\frac{dv_i}{d\tau} - \frac{du_i}{d\tau} - \frac{1}{10} a^2 \frac{d(\nabla^2 u_i)}{d\tau}}{\sqrt{\pi\nu(t-\tau)}} \tag{2.6}$$

where $x_{p,i}$ is the i-coordinate of particle position, m_p particle mass, v_i Lagrangian particle velocity, u_i Eulerian flow velocity, m_f mass of the volume of fluid occupied by the particle, $\frac{d}{dt}$ time derivative following a moving sphere, $\frac{D}{Dt}$ time derivative following the fluid particle, μ dynamic viscosity of fluid, g_i body force acting over particles.
The RHS of Eq.2.6 contains six terms: the first one is the buoyancy term due to the presence of gravity; the second represents the contribution to

the total force given by pressure gradient and viscosity for the case of undisturbed flow on an equivalent sphere of fluid; the third is the Coriolis term; the fourth is the added mass contribution, related to the time variation of the velocity field; the other two are respectively the Stokes drag force due to the disturbance produced by the presence of a particle in the flow and the Basset force that accounts for the unsteadiness of the viscous Stokes flow field.
Some terms are often small compared to the others, therefore not all the terms of Eq.2.6 are usually considered in the applications [14]: as an example, in aerosol applications, the density ratio could be $\frac{\rho_p}{\rho_f} \sim 700$, so that only Stokes drag force and buoyancy contribution affect particles trajectories. The Basset term and the added mass term are comparable with others in a fluid oscillating at a large frequency or in a starting from rest particle motion.

In the investigated case, the Lagrangian phase consists of tracers, representative of a particulate with inertia comparable with that of the carrying fluid and we can assume $\rho_f = \rho_p$. The dispersed phase is therefore treated as a swarm of fluid tracers, whose position is advanced in time just following:

$$\frac{dx_{p,i}(t)}{dt} = u_i = v_i \tag{2.7}$$

In this case, the forces acting on a fluid particle are already accounted in Eq.2.1 and Eq.2.2.

Chapter 3

The numerical method

3.1 The fundamentals of Large Eddy Simulation

In a in turbulent flow, various size vortices or rotating structures (called eddies) are present. The largest ones can be characterized by a length scale comparable to the dimension of the domain. The smallest ones has a size that is always larger than the molecular scales.

When the smallest scales present in the flow are sampled as in DNS approach, the most accurate description of the turbulent fluctuations is provided. Unfortunately, the computational cost (expressed both in terms of CPU time and variable storage) grows with a power of the number of Reynolds [11] and large or mid-scale problems (as for example the study of a coastal basin) result impossible to solve. A less expensive technique is Large Eddy Simulation. Larger scale structures of turbulence can be solved directly as in DNS approach and isotropic small scales are modeled.
To separate the large from the small scales, LES is based on the definition of a filtering operation: a filtered (or resolved, or large-scale) variable is here denoted by an overbar:

$$\bar{f}(x) = \int_D f(x')G(x, x'; \bar{\Delta})dx'$$

where D is the entire domain, G the filter function and $\bar{\Delta}$ the filter width determining the size of small scales structures. The filtering operation is applied to the governing equations to obtain the filtered equations of motion, which are solved in Large Eddy Simulation. For an incompressible flow of a Newtonian fluid, the filtered Eq.3.3 and Eq.3.4 take the form:

$$\frac{\partial \bar{u}_i}{\partial x_i} = 0 \tag{3.1}$$

$$\frac{\partial \bar{u}_i}{\partial t} + \frac{\partial (\bar{u}_i \bar{u}_j)}{\partial x_j} = -\frac{1}{\rho}\frac{\partial \bar{p}}{\partial x_i} - \frac{\partial \tau_{ij}}{\partial x_j} + \nu \frac{\partial^2 \bar{u}_i}{\partial x_j \partial x_j} \tag{3.2}$$

The effect of small scales appears through the subgrid scale term (SGS) $\tau_{ij} = \overline{u_i u_j} - \bar{u}_i \bar{u}_j$ that must be modeled.

Just because in Large-Eddy Simulations the dissipative scales of motions are resolved poorly or not at all, the main role of the subgrid scale model is to remove energy from the resolved scales, mimicking the drain that is usually associated with the energy cascade. It is important that the model represents the exact account for the effect of the subgrid stress.

In the eddy viscosity approach described by Germano et al. [15], the subgrid scale stress τ_{ij} is related to the large scale strain rate tensor $\bar{S}_{ij} = \frac{1}{2}\frac{\partial \bar{u}_i}{\partial x_j}\frac{\partial \bar{u}_j}{\partial x_i}$ according:

$$\tau_{ij} - \frac{\delta_{ij}}{3}\tau_{kk} = -2\nu_T \bar{S}_{ij}$$

with ν_T the eddy viscosity. In the Smagorinsky model the eddy viscosity is simply:

$$\nu_T = (C_s \bar{\Delta})^2 |\bar{S}|$$

with $C_s \simeq 0.18$ the Smagorinsky constant.

An LES subgrid model is the Dynamic Eddy viscosity Model (DEM) based on a dynamic subgrid scale approach [16]. In dynamic models the coefficient C_s is not a constant and it is evaluated by using the identity that in Cartesian coordinates reads as:

$$L_{ij} = T_{ij} - \tau_{ij}$$

where $L_{ij} = \widehat{\bar{u}_i \bar{u}_j} - \hat{\bar{u}}_i \hat{\bar{u}}_j$ are the resolved turbulent stress and $T_{ij} = \widehat{\overline{u_i u_j}} - \hat{\bar{u}}_i \hat{\bar{u}}_j$ is the subtest scale stress that appears when the test filter $\hat{.}$ with width $\hat{\bar{\Delta}} > \bar{\Delta}$, is applied to the filtered Navier-Stokes equations. The coefficient C_s is now:

$$C_s = -\frac{1}{2}\frac{< L_{ij} M_{ij} - N_{ij} M_{ij} >}{< M_{mn} M_{mn} >}$$

where $M_{ij} = (\hat{\bar{\Delta}})^2 |\hat{\bar{S}}| \hat{\bar{S}}_{ij} - \bar{\Delta}^2 \widehat{|\bar{S}|\bar{S}_{ij}}$ and $N_{ij} = (\widehat{\hat{\bar{u}}_i \hat{\bar{u}}_j} - \hat{\hat{\bar{u}}}_i \hat{\hat{\bar{u}}}_j) - (\widehat{\bar{u}_i \bar{u}_j} - \hat{\bar{u}}_i \hat{\bar{u}}_j)$. In Fig.3.1 a schematic representation of the energy spectrum is showed. The filter cut off at $\bar{k}$ defines the amount of energy that must be modeled in the term τ_{ij}; the test filter cut off is at $\hat{k}$.

Another LES subgrid model is the Dynamic Mixed Model (DMM) based on the scale similar approach [17]: the most active subgrid scales are those closer to the filter cutoff, and the scales with which they most interact are those above the cutoff [18]. The largest subgrid scales can be obtained by filtering the SGS velocity $u_i' = u_i - \bar{u}_i$ to get:

$$\bar{u}_i' = \bar{u}_i - \bar{\bar{u}}_i$$

If the SGS stress is decomposed in terms of $\bar{u}_i$ and u_i', and a Smagorinsky model is added to represent the dissipative effect of the small scales, the

stress model can be written as:

$$\tau_{ij} - \frac{\delta_{ij}}{3}\tau_{kk} = [\overline{\bar{u}_i\bar{u}_j} - \bar{\bar{u}}_i\bar{\bar{u}}_j - \frac{\delta_{ij}}{3}(\overline{\bar{u}_k\bar{u}_k} - \bar{\bar{u}}_k\bar{\bar{u}}_j)] - 2\nu_T\bar{S}_{ij}$$

The first part of the model is the scale similar one. The Smagorinsky contribution, computed dynamically, provides the dissipation that would have been underestimated by the scale similar part alone.

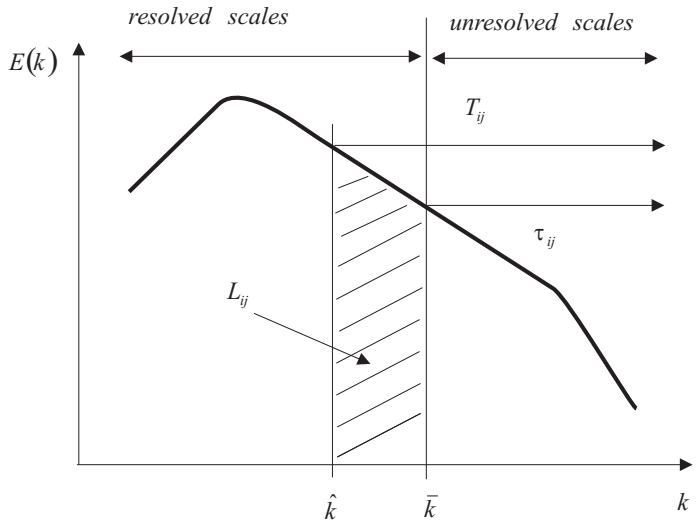

Figure 3.1: The picture schematically represents the energy spectrum and the relevant quantities in the LES approach.

3.2 The fractional step method of Zang, Street and Koseff.

In this section the most important features of the fractional step method are reported [19]. It has been implemented to solve the Eulerian phase, discretizing the three-dimensional, time-dependent incompressible Navier-Stokes equations in curvilinear coordinates.
The fractional-step method splits the numerical operators and achieves the coupling between pressure and velocity through solving a Poisson-like elliptic equation for pressure. Unlike other methods, the fractional step may be generally coupled with different choices of grid layouts. For example, either a staggered or non staggered grid may be used. Here the formulation with staggered grid is used: pressure and velocity are defined in the center of the computational cell, controvariant fluxes are on the faces center of the corresponding volume in the computational space. Velocity values in locations different from the center will be obtained via interpolation. In Fig.3.2 a sketch of a two dimensional grid layout for the computational variables is represented.

In this section a description of the numerical instrument core (the 3-D Navier-Stokes solver) is given, modified in order to run with both completely explicit or semi-implicit algorithms.
The computational grid can be defined in Cartesian and also curvilinear coordinates, necessary to follow flows developing in more complex geometry [20].

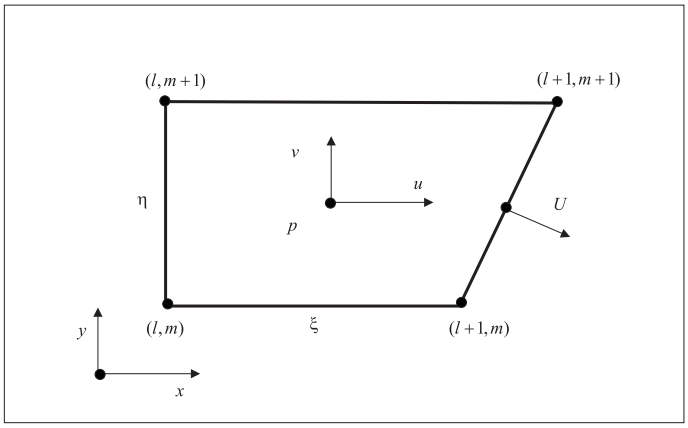

Figure 3.2: A computational cell in 2-D. The controvariant flux is indicated with U. Pressure and velocity are allocated in the center of the cell.

For sake of clarity, the Navier-Stokes equations are here rewritten in the case of constant viscosity ν and density ρ, according to the Einstein notation and omitting the terms that are relevant just in our particular applications

(the Coriolis contribute and the tidal forcing):

$$\frac{\partial u_j}{\partial x_j} = 0 \tag{3.3}$$

$$\frac{\partial u_i}{\partial t} + \frac{\partial}{\partial x_j}(u_j u_i) = -\frac{\partial p}{\partial x_i} + \nu \frac{\partial^2 u_i}{\partial x_j \partial x_j} \tag{3.4}$$

with $i, j = 1, 2, 3$; u_i represents a velocity component, p pressure divided by the fluid density. When the curvilinear coordinates $\xi_i = \xi_i(x, y, z)$ are used, these equations can be transformed in the form:

$$\frac{\partial U^m}{\partial \xi_m} = 0 \tag{3.5}$$

$$\frac{\partial (J^{-1} u_i)}{\partial t} + \frac{\partial F_i^m}{\partial \xi_m} = 0 \tag{3.6}$$

with the quantity

$$F_i^m = U^m u_i + J^{-1} \frac{\partial \xi_m}{\partial x_j} p - \nu G^{mn} \frac{\partial u_i}{\partial \xi_n}$$

where J^{-1} is the inverse of the Jacobian matrix determinant, representing the cell volume; U^m is the controvariant velocity multiplied by J^{-1} normal to the surface of constant ξ_m; G^{mn} is the mesh skewness tensor. In curvilinear coordinates, these quantities read:

$$U^m = J^{-1} \frac{\partial \xi_m}{\partial x_j} u_j$$

$$J^{-1} = det(\frac{\partial x_i}{\partial \xi_j})$$

$$G^{mn} = J^{-1} \frac{\partial \xi_m}{\partial x_j} \frac{\partial \xi_n}{\partial x_j}$$

The fractional step method proposed by Zang et al. in [19] follows a semi-implicit scheme for the time advancement, including the Adams-Bashforth method for the convective terms and the diffusive out of the diagonal ($i \neq j$ in our notation) and Crank-Nicolson for the diagonal diffusive terms [11]. For sake of clarity, here we define the time advancement scheme as provided by the two cited algorithms. When we consider a differential equation in the form:

$$\frac{du}{dt} = F(u, t)$$

with $F(u, t)$ a continuous function, we look for a solution via numerical integration [21]. The Adams-Bashforth explicit method refers to the following approximation:

$$\int_n^{n+1} F(t, u) dt \approx h(\frac{3}{2} F_n - \frac{1}{2} F_{n-1})$$

with h the time step.
Crank-Nicolson implicit method proposes:

$$\int_n^{n+1} F(t,u)dt \approx h(\frac{1}{2}F_{n+1} + \frac{1}{2}F_n)$$

We can therefore rearrange the continuity equation and the Navier-Stokes equation expressed in curvilinear coordinates in the form:

$$\frac{\delta U^m}{\delta \xi_m} = 0 \tag{3.7}$$

$$J^{-1}\frac{u_i^{n+1} - u_i^n}{\Delta t} = \frac{3}{2}(C_i^n + D_E(u_i^n)) - \frac{1}{2}(C_i^{n-1} + D_E(u_i^{n-1})) + R_i(p^{n+1}) + \frac{1}{2}(D_I(u_i^{n+1} + u_i^n)) \tag{3.8}$$

with R_i the discrete operator for pressure, D_E and D_I the discrete operators representing respectively the extra diagonal viscous terms treated in explicit way and the viscous ones treated in implicit way:

$$C_i = -\frac{\delta}{\delta \xi_m}(U^m u_i)$$

$$R_i = -\frac{\delta}{\delta \xi_m}(J^{-1}\frac{\delta \xi_m}{\delta x_i})$$

$$D_I = \frac{\delta}{\delta \xi_m}(\nu G^{mn}\frac{\delta}{\delta \xi_n}) \text{ with } m = n$$

$$D_E = \frac{\delta}{\delta \xi_m}(\nu G^{mn}\frac{\delta}{\delta \xi_n}) \text{ with } m \neq n$$

It is noteworth to say that the diagonal viscous terms ($m \neq n$) are treated in implicit way for the stability reasons [22]. Sec.3.2.1 is dedicated to the crucial problem of stability.

The fractional step procedure is also known as the predictor-corrector method: once a trial (or intermediate) velocity field is found, it will be corrected after the solution of the pressure.
The application of the fractional step method to Eq.3.8, leads to the following predictor-corrector solution procedure:

1. Predictor

$$(1 - \frac{\Delta t}{2J^{-1}}D_I)(u_i^* - u_i^n) = \frac{\Delta t}{J^{-1}}(\frac{3}{2}(C_i^n + D_E(u_i^n)) - \frac{1}{2}(C_i^{n-1} + D_E(u_i^{n-1})) + D_I(u_i^n)) \tag{3.9}$$

2. Corrector

$$u_i^{n+1} - u_i^* = \frac{\Delta t}{J^{-1}}(R_i(\phi^{n+1})) \tag{3.10}$$

where u^* is called the *intermediate velocity* which is not constrained by continuity. The quantity ϕ^{n+1} is a computational pressure connected to the same p and it is obtained by resolving the Poisson equation for pressure:

$$\frac{\delta}{\delta\xi_m}(G^{mn}\frac{\delta\phi^{n+1}}{\delta\xi_n}) = \frac{1}{\Delta t}\frac{\delta U^{m*}}{\delta\xi_m}$$

Note that the controvariant fluxes are present in the RHS.

In order to use the method, it is necessary to evaluate the LHS matrix in the predictor equation to obtain u^*. The scheme in use in the code can be summed up as follows:

1. Obtain u_i^* at the cell center by using the predictor.
   The inversion of the left term in the predictor equation is done via the approximate factorization therein described; once the predictor Eq.3.9 is rewritten in the form:

   $$(1 - \frac{\Delta t}{2J^{-1}}D_I)(u_i^* - u_i^n) = RHS \tag{3.11}$$

   then the factorization proceeds as:

   $$(1 - \frac{\Delta t}{2J^{-1}}D_I) = (1 - \frac{\Delta t}{2J^{-1}}(D_1 + D_2 + D_3))$$

   with $D_k = \frac{\delta}{\delta\xi_k}(\nu G^{kk}\frac{\delta}{\delta\xi_k})$ for $k = 1, 2, 3$.

   $$(1 - \frac{\Delta t}{2J^{-1}}D_1)(1 - \frac{\Delta t}{2J^{-1}}D_2)(1 - \frac{\Delta t}{2J^{-1}}D_3)(u_i^* - u_i^n) = RHS \tag{3.12}$$

   The inversion of the LHS term in Eq.3.12 asks for the resolution of tridiagonal matrices. This is an expensive step in terms of the computational cost. It can be avoided by keeping the resolution scheme in a completely explicit form.

2. Interpolate the values of u_i^* on the cells faces to obtain the controvariant fluxes and compute the RHS in the Poisson expression for pressure.

3. Resolve the pressure equation now that the RHS is known, and obtain a convergent value for ϕ^{n+1}.

4. Use the expression of the corrector to get u_i^{n+1} and the controvariant flux.

A consideration gets inside into the algebraic features of approximated factorization of Eq.3.12; when we opportunely rearrange Eq.3.11 in the form:

$$(1 - A_1)\hat{u} = RHS$$

with $u = (u_i^* - u_i^n)$ and $A_1 = \frac{\Delta t D_I}{2J^{-1}}$, we ask that

$$\hat{u} = (1 - A_2)u$$

with A_2 and u opportune matrices, mimicking the factorization of Eq.3.12 we obtain:

$$(1 - A_1)(1 - A_2)u = RHS$$

This factorization is second order accurate since:

$$(1 - A_1)(1 - A_2) = (1 - A_1 - A_2 + A_1A_2) \approx (1 - A_1 - A_2)$$

with A_1A_2 the second order term; this impose a limit to the accuracy expressed in the whole code: it is not possible to reach an order of accuracy higher than the second in time. Usually this is an acceptable condition for numerical simulations.

3.2.1 The stability problem.

The stability problem in a fluid dynamic code is determined by CFL condition (to be defined here and related to the convective term), by the viscous condition (related to the diffusive term) and interests the marching in time step Δt.

In order to determine the stability of an algorithm, it is possible to refer to Von Neumann method [21], whose essentials notes will be reported here for major clarity.
The method guarantees the necessary and sufficient condition for the stability in linear problems with initial conditions and constant coefficient.
In practical applications, the coefficients are frequentely non constant, the boundary conditions are usually complicated and the problems are non linear.
In this case the method can be applied locally (in our case in one cell), just in the points of the internal domain and the condition results only necessary and not sufficient.

The Von Neumann method provides the definition of the computational errors and the distribution along the grid at a time instant. The stability or the instability of an algorithm used for the computation is determined by considering that the Fourier component of the error can decade or amplify from a time step to the following one.

The error at the location x_j with j the node index in a one dimension grid is here defined as:

$$\xi_j^0 = \sum_{m=1}^{J-2} a_m exp^{i\theta_m j} \tag{3.13}$$

with $j = 2, 3, .., J-1$, $\theta_m = m\pi\Delta x$.

We assume that the error is periodic in the interval of interest Δx. According to the hypothesis of linearity it is possible to study the propagation of the error due to a single term of $exp^{i\theta_m j}$, therefore it is possible to omit the sum on the index m.

We define the gain function G as follows:

$$G = \frac{\xi_j^{n+1}}{\xi_j^n} \tag{3.14}$$

it represents the amplification factor of the error distribution. Von Neumann obtain a `general` criterion for stability: $|G| \leq 1$ for each θ.

In order to use this criterion and comprehend its role in our case, we can figure out a situation in which the diffusion is so important to reduce the unidimensional Navier-Stokes equation in the form:

$$\frac{\partial T}{\partial t} = \alpha \frac{\partial^2 T}{\partial x^2}$$

with T a passive scalar quantity as the temperature and α a diffusion coefficient; it can be discretized as follows:

$$T_j^{n+1} = sT_{j-1}^n + (1-2s)T_j^n + sT_{j+1}^n$$

with $s = \alpha\Delta t/\Delta x^2$ with Δx and Δt the discrete space interval and time step. By substituting in this equation the error definition of Eq.3.13 and using the gain criterion of Eq.3.14, it is possible to reach:

$$-1 \leq 1 - 4sin^2(\frac{\theta}{2}) \leq 1$$

and therefore $s \leq \frac{1}{2}$.
Therefore we can define the stability condition for the diffusion as:

$$\nu\frac{\Delta t}{\Delta x^2} + \nu\frac{\Delta t}{\Delta y^2} + \nu\frac{\Delta t}{\Delta z^2} < \frac{1}{2} \tag{3.15}$$

We consider now the transport equation written in the form:

$$\frac{\partial T}{\partial t} + u\frac{\partial T}{\partial x} - \alpha\frac{\partial^2 T}{\partial x^2} = 0$$

that can be discretized as follows:

$$T_j^{n+1} = (s + \frac{1}{2}C)T_{j-1}^n + (1-2s)T_j^n + (s - \frac{1}{2}C)T_{j+1}^n$$

where $s = \alpha\Delta t/\Delta x^2$ and $C = u\Delta t/\Delta x$.
We can derive the condition for a steady solution in the form:

$$0 \leq C^2 \leq 2s \leq 1$$

The local Courant number is defined as:

$$CFL = (\frac{|u_1|}{\Delta x} + \frac{|u_2|}{\Delta y} + \frac{|u_3|}{\Delta z})\Delta t$$

and in curvilinear coordinate it can be expressed as

$$CFL = (|U_1| + |U_2| + |U_3|)\frac{\Delta t}{J^{-1}}$$

with Δx,Δy,Δz the grid spacing and U_j the controvariant velocity. The new stability condition asks for:

$$max|CFL| \leq 1 \tag{3.16}$$

in all the computational domain. This guarantees that the displacement in one time step of a fluid particle can not be larger than the dimension of the cell containing it.

In conclusion, it is necessary to ensure that the choice of the time step Δt always guarantees both the stability conditions expressed in Eq.3.15 and Eq.3.16 in order to avoid a divergence in the computation.

3.2.2 A complete explicit form of the numerical code.

When we input the diagonal terms of Eq.3.8 resolved by the Crank-Nicolson scheme in those computed according the Adams-Bashforth algorithm, we obtain a simplification: it is no longer necessary to solve the factorized approximation, including matrices inversion and we can reduce the computational request in terms of CPU time. Referring to the RHS terms in Eq.3.8:

$$\frac{3}{2}(C_i^n + D_E u_i^n) - \frac{1}{2}(C_i^{n-1} + D_E u_i^{n-1}) + (D_I u_i^n)$$

in the completely explicit form, they read:

$$\frac{3}{2}(C_i^n + D_E u_i^n + D_I u_i^n) - \frac{1}{2}(C_i^{n-1} + D_E u_i^{n-1} + D_I u_i^{n-1})$$

It can happen that the time step Δt in the explicit formulation and in the semi-implicit one do not coincide because of the different algebra consequences on the stability condition. When the explicit time step results smaller, we need an higher number of iterations to get a desired convergence or to cover a requested time interval for the simulation. Therefore the reduced computational cost per time step can be vanished increasing the necessary number of iterations.

Both the schemes lead to the same numerical solution of a problem investigated. As a test, we report here the velocity profiles of two laminar fluxes whose analytic solution is known: the Poiseuille and the Couette ones.

The comparison is made with the numerical solution provided by the semi-implicit (S-I) and the complete explicit (E) advancement scheme.
Poiseuille flow is purely diffusive and when a channel of height h is considered, the vertical velocity profile reads:

$$u(z) = \frac{1}{2\nu}(\frac{\partial p}{\partial x})(z^2 - hz)$$

with ν the viscosity, p the pressure field, z and x the vertical and streamwise coordinate respectively. We develop a flow with $\nu = 1/100$ m^2/s, $h = 1$ m and a friction velocity $u_\tau = 0.031$ m/s. The domain is discretized with a $8 \times 8 \times 8$ grid. In Fig.3.3(a) the laminar profile $u(z)$ obtained analytically is compared with that obtained by the semi-implicit and the complete explicit scheme.
The Couette profile is determined by the relative motion of two parallel and infinite plates. In this case is not present a pressure gradient driving the flow in the streamwise direction ($\frac{\partial p}{\partial x} = 0$), and also the gradient $\frac{\partial u}{\partial x}$ vanishes. The vertical velocity profile reads:

$$u(z) = \frac{U_0 z}{h}$$

where U_0 is the fluid velocity at the upper plate. In our case $U_0 = 1$ m/s. It is noteworth that the profile does not depend upon the kinematic viscosity ν. The analytical Couette velocity profile is compared with that of S-I and E case in Fig.3.3(b).

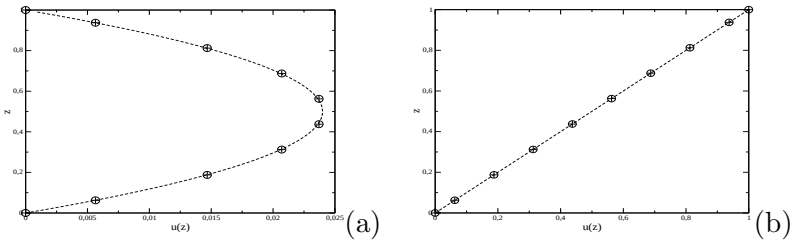

Figure 3.3: Laminar velocity profiles of Poiseuille on (a) and Couette on (b). Dashed lines is the analytic profile, circle is S-I case and plus is E case.

3.2.3 Scalability vs the numerical schemes

A parallel version of the numerical code above described exists. Written according the standard MPI [23], it is suited for the most common supercomputer architecture as Linux Clusters or IBM-Sp series. An extended description of the most important features characterizing the implementation is available on Cineca Science and Supercomputing reports [24]. Here,

some details regarding the problem of scalability as a function of the two numerical schemes described in Sec.3.2.2 will be given.

In principle, the possibility of using more than one CPU (parallel computing) to resolve numerically a problem is finalized in saving time and obtaining the same results of the serial computation (with only one computer devoted). An important parameter in this applications is the speed-up, that reads as the ratio between the computational time requested by a serial algorithm and that of the corresponding parallel one. Generally, the time spent in the computation tends to decrease as the number of CPUs in use increases. Correspondently, the speed-up tends to increase with the number of processors. In the reality this process, called scalability, is not linear because of the necessary data communication among the CPUs. Nevertheless, as the CPUs number grows, the time for the communication among them can become the determining parameter in evaluating the time necessary for the whole computation.
Therefore, in our case is crucial to evaluate *a priori* which is the most convenient scheme (E or S-I) to adopt before a new simulation starts and also which is the most convenient number of processors to use. These two data are dependent on the particular simulation and a generalization is not possible. In order to give a further intuition on this problem, in Tab.3.1 we report the time spent for one iteration in both the numerical schemes in use and the speed-up. These data are coming from a test simulation running on Linux Cluster at Cineca [25], in which the domain has been discretized with a $64 \times 64 \times 64$ grid. According the results provided, the most convenient number of CPUs to use is 16 coupled with the explicit scheme. No indications are exhibited on the length of the time step Δt.

	t_{S-I}	t_E	sp-up S-I	sp-up E
1 proc	9.80	9.40	***	***
2 procs	8.43	7.83	1.16	1.20
4 procs	4.52	4.10	2.17	2.30
8 procs	4.80	3.70	2.04	2.54
16 procs	2.50	1.10	3.92	8.54

Table 3.1: The mean value of the time t (expressed in seconds) necessary for a complete cycle (predictor and corrector) in one iteration and the speed-up are reported.

3.3 The interpolation

To perform applications involving turbulent flows with dispersed particles in the Eulerian-Lagrangian frame, a critical aspect is fluid velocity evaluation

at the instantaneous particle position, which in general does not coincide with one of the points of the grid containing the particle, so an interpolation of the fluid velocity field is required.

Interpolation techniques have been applied on both Cartesian and curvilinear grids [26], [27]. While in literature, interpolation techniques (*viz.* spectral, partial Hermite, Lagrangian, shape function methods, cubic splines etc.) have been extensively studied and applied on Cartesian grids [28], less effort has been devoted to the development of interpolation methods for non-Cartesian grids with boundary fitted curvilinear coordinates. Typically, the methods developed are linear and use different geometrical weighting procedures and produce similar interpolation functions in terms of performance and accuracy. Some of the procedures commonly in use are applicable only in two-dimensional meshes or may become impractical in Eulerian-Lagrangian simulations due to significant loss in accuracy when highly-distorted computational grids are used, others are based on iterative methods which require properly defined residuals to check the convergence of the solution [29].

Two are the most important features of an interpolator: it has to be accurate and fast. The level of accuracy can be determinate and increased by the number of grid points involved in the interpolation scheme. The swiftness of the interpolation procedure becomes relevant in terms of computational cost especially because the Lagrangian approach asks for a huge number of particles: normally an amount of $10^5 - 10^6$ trajectories have to be followed.

To overcome the restrictions connected to accuracy and swiftness, an interpolation scheme based on Taylor series expansion of fluid velocity, suited both for orthogonal and curvilinear grids has been implemented. Basically we refer to the interpolation scheme proposed by Marchioli et al. in [30].
Smooth functions can be approximated in the form a Taylor series expansion about a point where the exact value of it and its derivatives are known. Following this approach, the interpolation problem can be addressed within an Eulerian carrier scheme in which the fluid velocity components are available at spatially discrete grid nodes. Therefore the algorithm asks for the fluid velocity at the cell node $N(x, y, z)$ closest to the particle to estimate the local fluid velocity at instantaneous particle position $P = (X, Y, Z)$.

For each particle, in the simple case of Cartesian coordinates, considering only the terms up to the first order, the Taylor series approximating the fluid velocity at particle postion reads:

$$u_i|_P = u_i|_N + \frac{\partial u_i}{\partial x}|_N(X - x) + \frac{\partial u_i}{\partial y}|_N(Y - y) + \frac{\partial u_i}{\partial z}|_N(Z - z) + O(X_i - x_i)^2 \tag{3.17}$$

with $u_i|_P$ the fluid velocity at particle position and $u_i|_N$ the fluid velocity at the node closest to the particle.
The truncation error is $O[(X_i - x_i)^2]$ consistent with that of the numerical

scheme in use for the resolution of the Eulerian velocity field.
In curvilinear structured grids, the Navier-Stokes equations are solved in a computational space, whose coordinates are denoted with $\xi_i = (\xi, \eta, \zeta)$. For sake of clarity we report here how the derivatives are consistently transformed:

$$\frac{\partial u_i}{\partial x_j} = \frac{\partial u_i}{\partial \xi_k}\frac{\partial \xi_k}{\partial x_j} = \frac{\partial u_i}{\partial \xi}\frac{\partial \xi}{\partial x_j} + \frac{\partial u_i}{\partial \eta}\frac{\partial \eta}{\partial x_j} + \frac{\partial u_i}{\partial \zeta}\frac{\partial \zeta}{\partial x_j}$$

with $i, j, k = 1, 2, 3$.
And therefore the implemented interpolation scheme reads:

$$u_i|_P \simeq u_i|_N +$$
$$[\frac{u_i^{l+1} - u_i^{l-1}}{2\Delta\xi}\frac{\partial \xi}{\partial x}|_N + \frac{u_i^{m+1} - u_i^{m-1}}{2\Delta\eta}\frac{\partial \eta}{\partial x}|_N + \frac{u_i^{n+1} - u_i^{n-1}}{2\Delta\zeta}\frac{\partial \zeta}{\partial x}|_N](X - x) +$$
$$[\frac{u_i^{l+1} - u_i^{l-1}}{2\Delta\xi}\frac{\partial \xi}{\partial y}|_N + \frac{u_i^{m+1} - u_i^{m-1}}{2\Delta\eta}\frac{\partial \eta}{\partial y}|_N + \frac{u_i^{n+1} - u_i^{n-1}}{2\Delta\zeta}\frac{\partial \zeta}{\partial y}|_N](Y - y) +$$
$$[\frac{u_i^{l+1} - u_i^{l-1}}{2\Delta\xi}\frac{\partial \xi}{\partial z}|_N + \frac{u_i^{m+1} - u_i^{m-1}}{2\Delta\eta}\frac{\partial \eta}{\partial z}|_N + \frac{u_i^{n+1} - u_i^{n-1}}{2\Delta\zeta}\frac{\partial \zeta}{\partial z}|_N](Z - z) \quad (3.18)$$

where index spaces $L(l, m, n)$ identifies the cell node $N(i, j, k)$ in the curvilinear coordinates system. As previously discussed, the choice of the computational time step, due to the stability conditions [22], does not allow a particle to pass more than one cell per iteration. Thus the node $N(i, j, k)$ at the following iteration can be the same or could be found just around the surroundings $N(i, j, k)$ at the present iteration. This reduces the variability in the node research for the algorithm implemented.

In order to achieve particle position, Eq.2.7 is integrated by means of an explicit, second order accurate Adams-Bashforth scheme:

$$x_{p,i}^{n+1} = x_{p,i}^{n} + \Delta t(\frac{3}{2}v_i^n - \frac{1}{2}v_i^{n-1})$$

where Δt is the time step that guarantees the stability conditions of Sec.3.2.1.

3.3.1 The interpolator testing

Among the tests for the validation of our interpolation model, the most meaningful is reported in this section. We consider a single fluid particle and originally place it in a known position of the domain. We impose a free vortex fluid velocity field in the domain discretized with a curvilinear and Cartesian grid (Fig.3.4(a) and (b) respectively). The imposed velocity field reads:

$$u(x, y, z, t) = u_0$$
$$v(x, y, z, t) = -v_0(z - C)$$

$$w(x, y, z, t) = w_0(y - C)$$

where C is a constant, (u, v, w) are the three velocity component along x, y, z directions respectively, and u_0 is the initial velocity values in the streamwise direction, v_0 and w_0 are the two reference frequency of the free vortex. The projection on the plane $y - z$ of the velocity field is represented in Fig.3.5(a) with vectors whose length indicates the amplitude of the velocity field and where the arrows indicate the direction of motion. The trajectory of a tracer subjected to the imposed velocity field is reported on Fig.3.5(b). Because of the relatively simplicity of the imposed velocity field, we are able to analytically predict the evolution of particle position by integrating its equation of motion and therefore check if the particle is correctly accelerated along its time evolution in the domain. As observed in Fig.3.6, where the evolution in time of the three components of the particle position are shown, no appreciable difference is present in the particle postion when both a curvilinear and a Cartesian grid discretize the domain: this is guaranteed by the formulation of the interpolation scheme in Eq.3.18, suited for both cases.

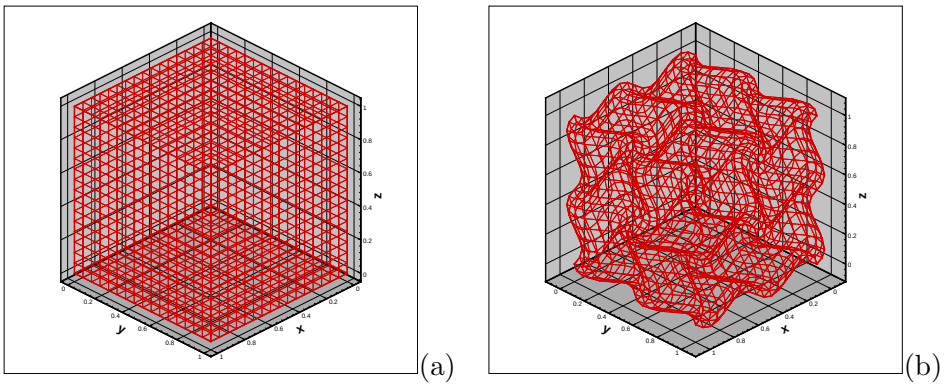

Figure 3.4: Example of a grid used for test simulations. Cartesian coordinates grid on (a) and curvilinear on (b).

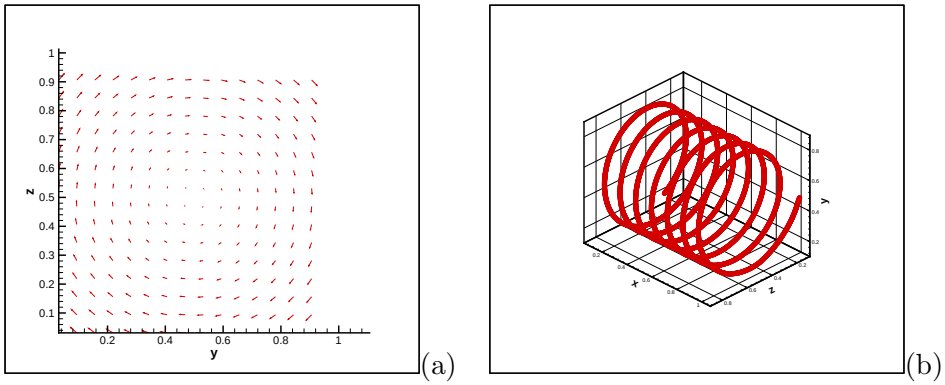

(a) (b)

Figure 3.5: In (a) the velocity field in a plane orthogonal to the streamwise direction is represented. The amplitude is proportional to the vector length. In (b) the trajectory of a particle developing in time according to the imposed velocity field is shown.

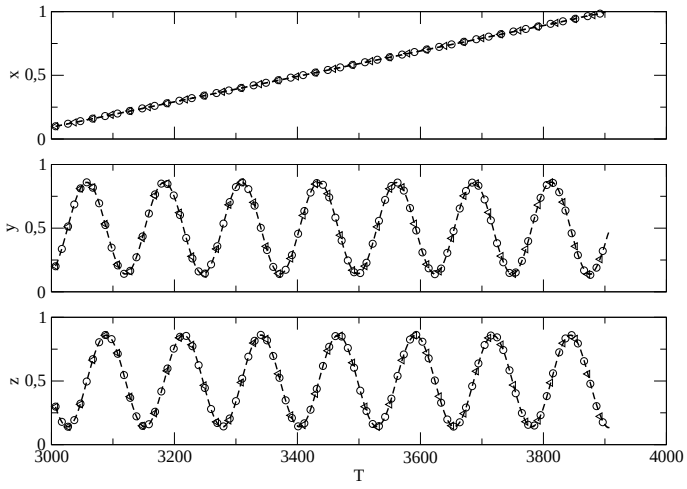

Figure 3.6: The time evolution of the three coordinates of the particle positions subjected to the imposed free vortex velocity field is shown. Dashed lines represent the analytic solution, circle represent the case in which a Cartesian grid discretizes the domain and left triangle the case with a curvilinear grid.

3.4 A subgrid model for the Lagrangian phase

In this section we enforce the importance of the evaluation of the velocity field for the dispersed phase as depending on the carrying fluid velocity. This is not a trivial point for the simple reason that a numerical approach where all the scales are completely resolved is not always possible and the consequent use of parameterization or modeling can lead to a lack of information in the resulting Eulerian and Lagrangian velocity field. In the case of LES, this problem gives rise to the born of subgrid models [31], that have the role of recover the lack of information lost with the filtering approach discussed in Sec.3.1: in an LES, the fluid field is filtered to split the motion of larger eddies from the smaller ones; the larger scales of the turbulent flow are explicitly simulated, while the effects of the smaller subfilter scales are modeled.

Dealing with particle dispersion in LES simulation, different sources of error can be distinguished with respect to DNS: a modeling error, because an LES does not provide the exact fluid velocity but only an approximation caused by the limitations of the subgrid model; a subgrid error, because the particle equations are solved with the filtered velocity; an interpolation error, because the particle location usually does not coincide with the grid nodes and an interpolation scheme is needed.
The problem concerning the interpolation scheme has been already discussed in Sec.3.3 and the approach we use, whose accuracy corresponds to that of the Navier Stokes solver, has been properly refereed [30].
A recent approach to the problem of Lagrangian dispersion when LES techniques are used for the continuous phase, lays in the defiltering of the filtered variables, that will ensure the reconstruction of the filtered signal. This allows to face the problem of the subgrid modeling. Among the others, the defiltering based on deconvolution techniques has already been used directly for the Eulerian phase by Stolz and al. [32], but any direct application on the Lagrangian tracking was provided.
Dealing with the problem of subgrid error, here we consider the deconvolution method proposed by Kuerten [33] and reproduce it in our numerical model. In this case the model has the specific goal of ensuring the best velocity field available for the Lagrangian tracking when LES techniques are in use for the Eulerian phase.

For sake of clarity, some notes on the mathematical definition of deconvolution are here reported. Being two signals as function of space $f(x)$ and $G(x)$, the convolution $h(x)$ between them is defined as [34]:

$$f(x) * G(x) = \int_{-\infty}^{+\infty} f(x' + x)G(x')dx' = h(x) + \varepsilon$$

with ε the noise. The inverse for f of the convolution equation is the decon-

volution of the signal:

$$[h(x) + \varepsilon]G(x)^{-1} = f(x)$$

In our case the signal is the Eulerian velocity field, G is the LES filter and the deconvolution model provides the reconstruction of the instantaneous (unfiltered) velocity $u_i = \bar{u}_i + u_i^{'}$ from the resolved one $\bar{u}_i$.
If the filter function G used in the LES is invertible, deconvolution becomes trivial, since it simply consists of the application of the inverse filter G^{-1} to $\bar{u}_i$.
The main difficult involved in deconvolution lays in the fact that filters with the desired support in the Fourier space are non-invertible, or generally, with not unique inverse, since their application results in loss of information. This implies that the deconvolution can only be approximate, in the sense that one can obtain an approximation u_i^* of the total velocity u_i from the resolved one $\bar{u}_i$ [35]. In principle, when the approximated u_i^* is given, the subgrid stress could be modified directly in terms of the estimated total velocity as:

$$\tau_{ij} = \overline{u_i^* u_j^*} - \overline{u}_i^* \overline{u}_j^*$$

and this was present in the numerical approach of Stoltz et al. [32].

As in the case of the interpolation scheme in Sec.3.3, a definition of deconvolution comes from the Taylor series: an inverse filter operator Q_N is defined as a truncated series of filtering operations:

$$Q_N = \sum_{n=1}^{N} (I - G)^n \simeq G^{-1}$$

with I the identity operator. Using this equation, the approximate deconvolution velocities u_i^* can be obtained by applying the filter as:

$$u_i^* = \sum_{n=0}^{N} (I - G)^n \bar{u}_i = \bar{u}_i + (\bar{u}_i - \bar{\bar{u}}_i) + (\bar{u}_i - 2\bar{\bar{u}}_i + \bar{\bar{\bar{u}}}_i) + ... \qquad (3.19)$$

Following Kuerten approach, in our numerical model we reconstruct the defiltered velocity field using the first two terms in the RHS of Eq.3.19 (being consistent with the accuracy of the Navier Stokes solver in use), and we use this new velocity field as an input for the interpolation scheme of Eq.3.18.

3.4.1 The subgrid model testing

As in the case of the interpolation scheme proposed by Marchioli et al. [30] the Kuerten subgrid model for particles [33] has been already tested and opportunely refereed. Therefore the results we report here have to be intended as related to our implementation of the numerical method [36].

We face a problem of particulate dispersion in a channel flow. The case investigated has been previously considered in a Benchmark simulation [37]; in that case, the Eulerian velocity field was resolved with the DNS approach. This allows a comparison with our results obtained via LES.

The dimensions of the considered channel flow are $L_x = 4\pi\delta$, $L_y = 4/3\pi\delta$ and $L_z = 2\delta$ and with high dimension $h = 2\delta = 0.04$ m. The mean flow is in the $x-$axial direction, with mean velocity varying above all in the cross-stream direction. Periodicity is considered in the streamwise and spanwise directions; a particle that reaches the upper or the bottom planes will be stopped. Gravity force is not considered, therefore a symmetry in the flow statistics by $y = \delta$ plane is aspected. Fluid parameters are: $Re_\tau = 150$, with the friction velocity $u_\tau = 0.11775$ m/s, density $\rho_f = 1.3$ kg/m^3 and kinematic viscosity $\nu = 1.57\ 10^{-5}$ m^2/s. A number of $102,400$ particles has been considered, initially divided in 16 wall normal planes of 80×80 particles each. Particles parameters are: density $\rho_p = 1000$ kg/m^3, Stokes number $St = 1$ defined as the ratio between the particle relaxation time $\tau_p = \rho_p(2a)^2/18\mu$ and the time $\tau_f = \nu/(u_\tau)^2$ characteristic of the continuous phase, and μ the dynamic viscosity. We run a parallel computation with 16 CPUs and the S-I scheme.

The problem has been treated according the Eulerian-Lagrangian approach and, by considering the simulation parameters, it is possible a simplification of Eq.2.6, neglecting the terms that have a small contribute [14]. As explicitely requested for the Benchmark simulation [37], Maxey and Riley equations have been rearranged in the form that accounts for the Stokes term only:

$$\frac{dx_{p,i}}{dt} = v_i \tag{3.20}$$

$$\frac{dv_i}{dt} = \frac{u_i - v_i}{\tau_p}(1 + 0.15Re_p^{0.687}) \tag{3.21}$$

with $x_{p,i}$ and v_i particle position and velocity, u_i the fluid velocity and Re_p the particles number of Reynolds.

The Eulerian velocity field has been resolved using the different techniques indicated on Tab.3.2. DNS data are provided by the Benchmark simulation database. In our LES approaches we discretize the domain by means of a stretched grid, ensuring that the smallest structures present near the wall are resolved up to $z^* = \nu/u_\tau$. This quantity is used for the normalization of the length of interest in the statistics, while the friction velocity is used for the normalization of the velocity. LES-1 uses the dynamic eddy-viscosity SGS model (DEM) of Sec.3.1. LES-2 uses the dynamic mixed model (DMM) of Sec.3.1. LES-3 uses the previous dynamic mixed model and the deconvolution modules (DMM-D) described in Sec.3.4.

We first analyze the Eulerian velocity field. In particular, first order (the mean) and second order (the root mean square) statistics of the velocity are

Numerical Technique	Grid	Time
DNS	$128 \times 128 \times 128$	n.a.
LES-1 DEM	$64 \times 96 \times 64$	1.2 sec
LES-2 DMM	$64 \times 96 \times 64$	1.3 sec
LES-3 DMM-D	$64 \times 96 \times 64$	1.5 sec

Table 3.2: Computational methods and the grids used for the problem of particles dispersion. The time per iteration on parallel machine, when available, is also reported.

here reported in the half channel. Fig.3.7(a) shows that the Eulerian mean velocity component in the streamwise direction is correctly represented in LES models when compared to DNS. The behavior of the root mean square velocity components of the continuous phase are reported in (b),(c) and (d). In the case of the spanwise and wall normal directions, that are non directly interested by the bulk flow, the LES approaches are not able to reproduce the whole energy amount because of the filter operation. This remains true even when the subgrid terms are currently added to the statistics (the case is indicated with DMM+sgs).
This suggests the importance of the subgrid model implemented for the Lagrangian phase. Our intent is to get round the subgrid error discussed in Sec.3.4 and evidenced by the statistics here reproduced: once the Eulerian phase is resolved by the Large Eddy approach, a deconvolution model can recover the energy lost in the filtering and provide a correct velocity field for the interpolation scheme described in Sec.3.3.
Fig.3.8 shows on (a) the mean velocity of particles in the streamwise direction and the second order statistics in the three directions on (b),(c) and (d) respectively. In the comparison, also the statistics obtained from a dynamic-inverse model [38] present in the Benchmark database have been added. As showed in Fig.3.8(a), this model overestimates the mean velocity component as soon as the wall region is leaved. In comparison with DNS, the best results in terms of error percentage are those in which the deconvolution model of Sec.3.4, is added to the DMM approach of Sec.3.1 for the continuous phase. A difference still exists and can be explained with this argumentation: the deconvolution, as the inverse of the convolution operation, takes with itself an error [34] to be added to the others indicated (*i.e.* the interpolation, the modeling of particles equations and the filtering of the momentum equations). Even if the subgrid contributions are recovered just in a statistics sense, our results guarantees that the largest part of the energy amount lost in the filtering has been recovered and therefore the described approach can be considered as an useful research instrument for dispersion problems in the fluid dynamics.

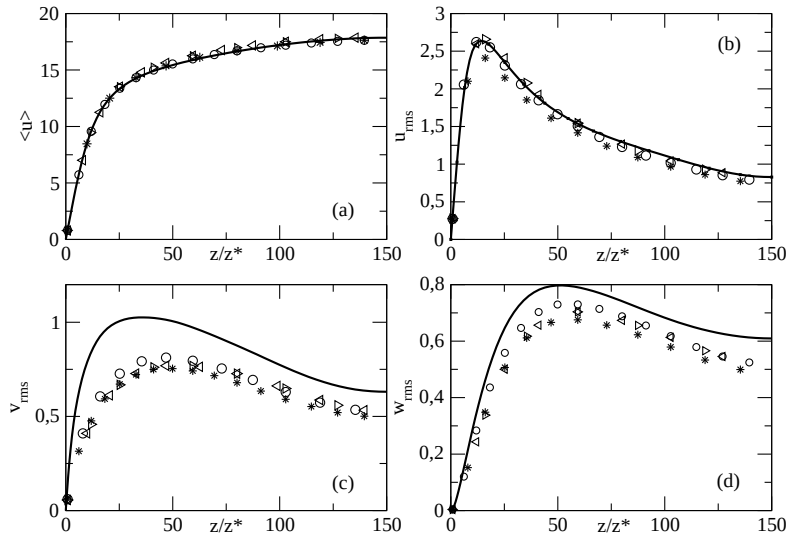

Figure 3.7: First and second order velocity statistics of the Eulerian field. Left triangle is DEM + SGS; right triangle is DEM; star is DMM; circle is DMM + SGS; straight line is DNS

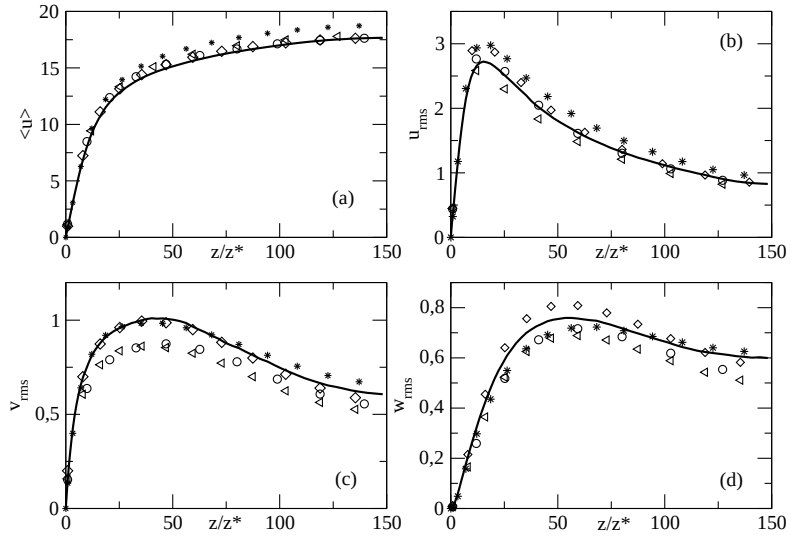

Figure 3.8: First and second order velocity statistics of particles. Left triangle is DEM; circle is DMM; diamond is DMM-D; star is dynamic-inverse; straight line is DNS.

Chapter 4

Results and discussion

4.1 The investigated case

In the present work we refer to parameters typical of a real mid-latitude problem (*i.e.* data of the Gulf of Trieste, northern Adriatic Sea, see Fig.1.2). Consistentely with the description provided in Sec.1.2, we assume that the driving current is dominated by the M2 tidal component ($T_{M2} = 12.42$ hours) and our reference value for the free stream velocity is $U_0 = 0.05$ m/s. The mean water depth is 16 m, the viscosity of water is $\nu = 1.15 \times 10^{-6}$ m^2/s and the latitude is $\phi = 45^o$. We obtain the following parameters:

$$KC = \frac{U_0 T_{M2}}{h} = 140 \qquad Re_S = 5560 \qquad Ro = 1.36$$

.

As discussed by Salon [39], when the friction Reynolds number is evaluated from the case of $Re_{M2} = 15 \times 10^6$, a value of $Re_\tau = u_\tau h/\nu = 24600$ is obtained. Due to the fact that the actual value of the friction Reynolds number is well beyond the present ability of simulation techniques like direct simulations (DNS) or *resolved* Large Eddy Simulation (LES), in the present work we refer to the Reynolds number $Re = 1.6 \times 10^6$ corresponding to $Re_S = 1790$ (*i.e.* $Re = Re_S^2/2$), and guaranteeing that at this Reynolds number the turbulent regime is present in the most part of the cycle [40].

In this work one period of the oscillating flow was reproduced via LES. The simulations were carried out over a rectangular box, using periodic conditions on the horizontal planes of homogeneity, a stress-free condition at the top boundary and a no-slip condition at the bottom solid wall. The depth of the domain and the amplitude of the free stream velocity were scaled holding the full scale value of KC, whereas the horizontal dimensions of the computational domain were chosen large enough to accurately reproduce the largest scales of the motion. The computational parameters used for the simulations of the Eulerian field are in Tab.4.1.

	$L_x/\delta_S, L_y/\delta_S, L_z/\delta_S$	n_x, n_y, n_z	$\Delta x^+, \Delta y^+, \Delta z^+_{min}, \Delta z^+_{max}$
OF	$50, 25, 40$	$64 \times 64 \times 256$	$62, 31, 2, 22$
OFR	$50, 50, 40$	$64 \times 128 \times 256$	$62, 31, 2, 22$

Table 4.1: Computational parameters of the simulations at $Re_S = 1790$. The non-dimensional grid spacing is referred to the maximum wall shear stress along the period and consequently to the minimum value of the wall unit $z^* = \nu/u_\tau$. OF refers to the purely oscillating flow, OFR refers to the oscillating flow in the case with rotation.

The simulations were executed in two distinct cases. First we considered the dispersion of a swarm of particles in the case of a purely oscillating flow (Stokes boundary layer) in the turbulent regime (OF in Tab.4.1), subsequently we moved particles in the oscillatory rotating flow (Stokes-Ekman boundary layer; OFR in Tab.4.1), with the aim to quantify the effect of rotation on the characteristics of particulate dispersion for a mid-latitude shallow-water environment. In both cases $102,400$ tracers were released in the flow field. Particles were initially placed over 16 longitudinal planes $x_1 - x_3$, respectively using for each plane 80×80 particles. A DMM, S-I scheme was adopted for the Eulerian phase coupled with the deconvolution model of Sec.3.4 for the Lagrangian tracking. As regards the initial conditions of the simulations, a statistically steady Eulerian field was considered at the phase $\theta = 0^\circ$ and particles were released in the Eulerian field with velocity equal to that of the carrying fluid.

For sake of clarity, we give here some meaningful details on the Eulerian phase, referred to a previous investigation of Salon et al. [41] where five periods of oscillation have been simulated and a comparison with the results of a work of Jensen et al. [42] was possible. In Fig.4.1(a) is shown the evolution of the velocity streamwise component at the free surface in both OF and OFR cases. This trend is consistent with that imposed by the tidal forcing expressed in Eq.1.2 and no differences are appreciated when the frame of reference changes. At the value of Ro herein considered, the oscillating-rotating boundary layer presents notable differences with its non-rotating counterpart: as known, the Coriolis force gives rise to a cross-stream pressure gradient that develops a non-zero mean spanwise velocity which is not observable in the non-rotating case of Fig.4.1(b).

As observed in Fig.4.2, where the streamwise and spanwise velocity profiles are reported, due to the combined effect of oscillation and rotation, an oscillating spanwise velocity develops. During the steady oscillation, its intensity is one order of magnitude smaller than that of the streamwise component. In this case we are analyzing the whole fluid column, and not only the free surface as in the data of Fig.4.1(a). We notice that rotation also affects the streamwise velocity component. This clearly appears in the

ensemble-averaged vertical profiles plotted in Fig.4.2, that shows how significant differences in $< u >$ between the OF and the OFR cases are present along the whole water column. It is noteworthy that the bulge characterizing the mean profile of $< u >$ both in the laminar [43] and in the turbulent Ekman layer [44] and also in the OF case, is practically absent in the rotating case. The streamwise velocity mean profiles of the central phases (between 60° and 150° and between 240° and 330° in Fig.4.2) are monotonic in z and are associated to values of the Reynolds shear stresses $< u'w' >$ (see Fig.4.3) nearly constant especially in the core fluid, signature of activity of the mixing processes that is not limited to the wall region. As a result of enhanced mixing, the gradient of the mean streamwise velocity profile does not exhibit a change of sign and consequently the Reynolds shear stress $< u'w' >$ maintains its own sign along the water column.
The presence of the horizontal components of the Coriolis force thus increases turbulence in the flow field [44].

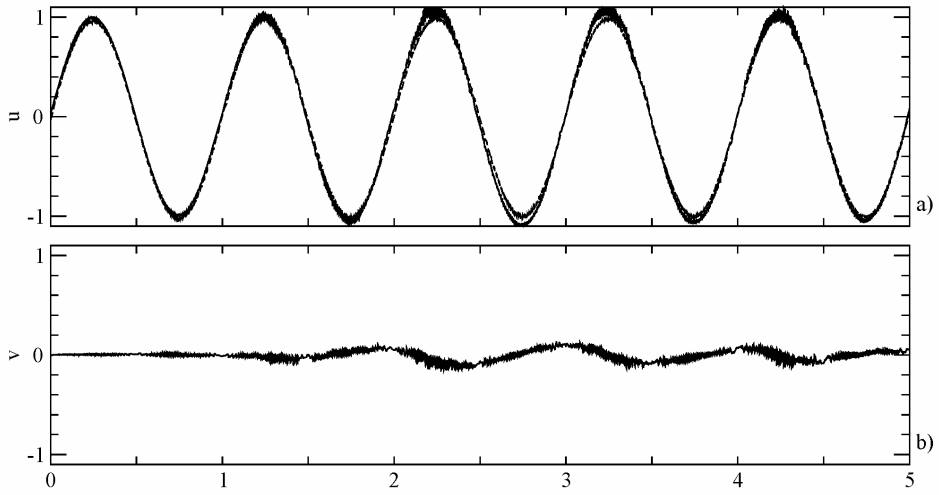

Figure 4.1: Temporal evolution along the first 5 periods of oscillation of the horizontal components of the resolved velocity at the top of the domain: a) streamwise velocity in OF (dashed line) and OFR (solid line) cases; b) spanwise velocity in OFR case. Note that the last variable is zero in the OF case.

Another important effect is the breaking of symmetry either in the velocity profiles (Fig.4.2) and in the Reynolds stress (Fig.4.3) between the two half cycles of oscillation. Specifically, this effect well explained in Salon et al. [41] and in the literature there reported, is due to the sign change throughout the cycle of oscillation of the horizontal mean vorticity related to the mean vertical shear stress, with respect to the background vorticity. In

particular, during the decelerating phases of the second half cycle (between 300° and 345°) the Reynolds stress are more intense that what measured during the corresponding phases of the first half cycle. Consistently with the literature [44], we observe in our simulations the East/West enhancement/reduction trend that explains how, in the Northern hemisphere, forcing coming from East (associated with a mean shear vorticity anti-parallel to the background vorticity) tends to destabilize the turbulent field, whereas a forcing coming from West (with mean vorticity parallel to the background one) tends to stabilize it.

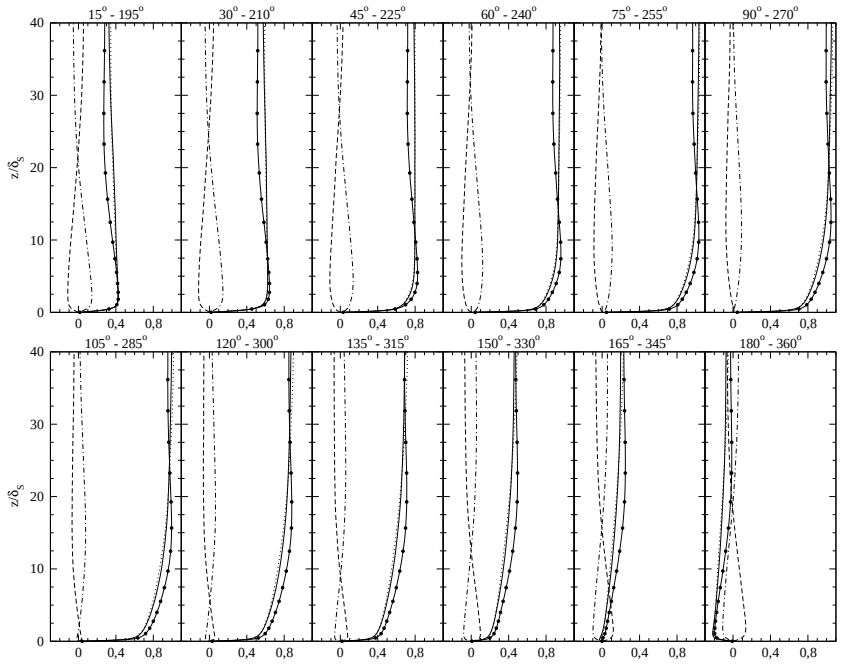

Figure 4.2: Evolution along the 24 phases of oscillation of the vertical profile of the mean streamwise velocity $< u >$ in the OF case between 0° and 180° (solid line with dots), of $< u >$ in the OFR case between 0° and 180° (solid line), of $- < u >$ between 195° and 360° (dotted line, the sign is opposite for sake of clarity) and of the mean spanwise velocity $< v >$ for the OFR case between 0° and 180° (dashed line) and between 195° and 360° (dashed-dotted line). The values are made non-dimensional with U_0.

In particular, we will evidence that, even if rotation does not vary the amount of energy in the system, it can extract energy from the mean flow to enhance turbulent activity in the fluid column: the Coriolis force originates a spanwise pressure gradient that gives a non zero mean cross stream velocity, smaller in magnitude than that in the streamwise direction due to the presence of the oscillatory tide. As indicated in Sec.1.3, fluid particles tend

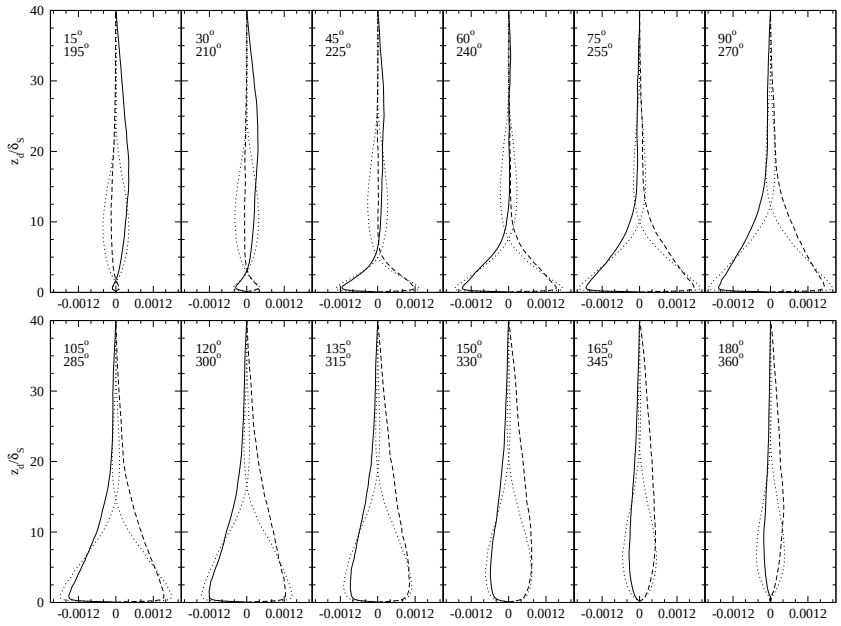

Figure 4.3: Evolution along the 24 phases of oscillation of the vertical profile of the mean Reynolds shear stress $< u'w' >$ for the OF case between 0° and 360° (dotted line), for the OFR case between 0° and 180° (solid line) and between 195° and 360° (dashed line). The values are made non-dimensional with U_0^2.

to travel on elliptical trajectories and the ratio between their axes varies with the distance from the wall.

Our numerical approach allows to recognize three distinct regions in the water column: a near-bottom wall one characterized by small-scale turbulent structures, a free surface region, where turbulent mixing is weaker and last, a core intermediate region. The vertical mixing due to turbulence is enhanced by the presence of rotation that enlarges the size of the first zone.

The approach in use allows to calculate explicitly the particle turbulent diffusivity. As theorized by Taylor, it is observed to depend upon the time according the two classical ballistic and Brownian regimes.

4.2 Particle dispersion in the turbulent oscillating flow field

The Eulerian phase of the turbulent Stokes boundary layer at $Re_S = 1790$ was also analyzed and discussed in [45] and in the literature therein reported. We summarize some results relevant for the present discussion.

The oscillatory boundary layer is inherently unsteady, and presents a symmetry between the first ($0^o \div 180^o$) and the second ($180^o \div 360^o$) half cycle which, in a statistical sense, repeats identically to the first one, apart that the sign of the streamwise velocity is inverted. The half cycle is characterized by two main phases, namely the phase of acceleration from 0^o to 90^o and a successive phase of deceleration, up to 180^o. The study presented the following scenario: during the late deceleration up to the early acceleration phases, a thin laminar boundary layer develops. At $Re_S = 1790$ this boundary layer undergoes a transition due to shear instability between 30^o and 45^o accompanied by a sharp increase of the turbulent kinetic energy K, related to the rapid growth of the production rate of K. Fully developed, equilibrium turbulence is observed between 60^o and around 150^o, when the mean velocity profiles are characterized by the presence of a log-layer and the flow dynamics evolves through a sequence of quasi-equilibrium states. In the early to mid deceleration phases a strong turbulence dissipation is observed related to the explosive, bursting production of small scale vorticity (see also [46]). Around 160^o the flow field starts to stop and invert its own direction, first in the near-wall region and subsequently upward in the fluid column. This inversion produces the splitting of the fluid column into two separate regions, a near-wall one where a laminar boundary layer rapidly grows, and an upward one where turbulence has strongly decayed owing to the absence of production rate and, due to a history effect, few large-scale structures coming from the previous phases populate the fluid column. The study has also shown that, at $Re_S = 1790$ significant turbulent activity is detectable in the fluid column up to $25\delta_S$.

Fig.4.4 shows the 3D trajectories of selected particles released at two

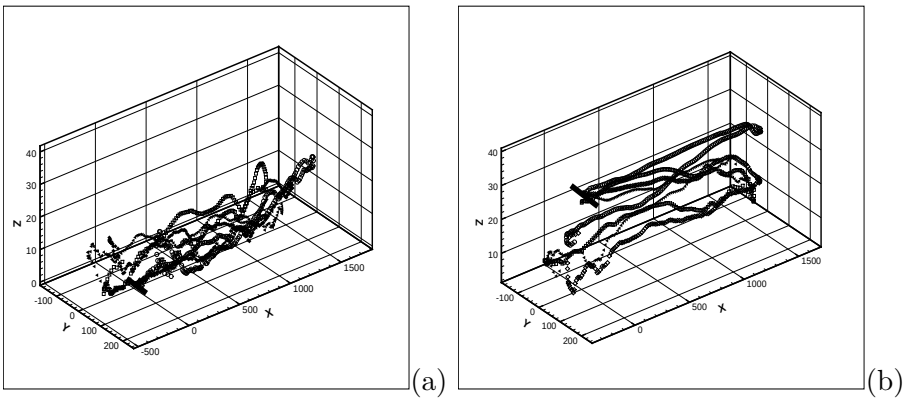

Figure 4.4: Trajectories of particles along an oscillatory cycle, released at a fixed horizontal station (plotted as a thick segment) at two different heights in the fluid columns: a) $z = \delta_S$; b) $z = 30\delta_S$. For sake of clarity, the ratio among axis is exaggerated and the ticks are in δ_S units.

different heights in the flow field; on (a) the trajectories of particles released in the near-wall region show the presence of turbulent mixing during most of the first half cycle of oscillation. The particles undergo a large scale motion during the phases of inversion (around 180^o) and again they are subjected to a wide spectrum of turbulent scales during the second half cycle. Conversely, on (b) particles released above the turbulent region have trajectories that do not exhibit the presence of significant turbulent mixing. In all cases, during the phases when inversion of the flow direction takes place (160^o-180^o), particles are subjected to a very large scale displacement in the cross-stream direction, which tends to transport them at a fast rate within the fluid column. As shown in [45], this transport cannot be associated to classical turbulent mixing, since at the inversion phases turbulence is nearly suppressed in the near-wall region and only few large-scale structures populate the flow field. However, these weak large-scale structures are able to transport the dispersed phase over distances comparable with their length scale in the flow field and consequently they still supply a source of mixing for the particulate.

We split the computational box in 10 horizontal slabs (with thickness equal to $4\delta_S$), catch the particles originally placed in each slab and follow them along their evolution in the cycle simulated. In Fig.4.5 we observe that the mean vertical displacement of the particulate rapidly increases for particles released in the near-wall region, due to the large mixing. The mean vertical displacement of the particles gradually reduces for particles initially released in the core region of the turbulent layer, associated to nearly symmetric vertical fluctuations, whereas particles released in the free surface region on average tend to be transported toward the wall. This

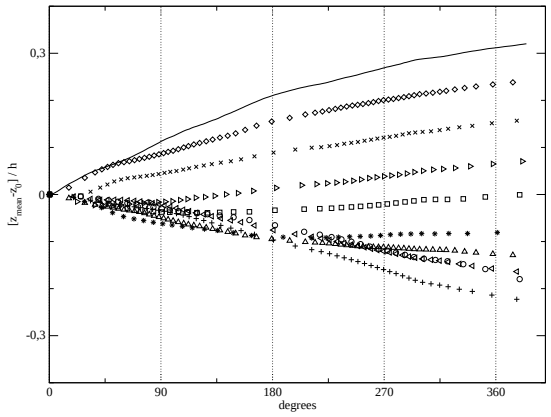

Figure 4.5: Mean non dimensional vertical displacement of tracers originally released at different heights from the wall in the OF case: $0.0-0.1$ (solid line); $0.1-0.2$ (diamond); $0.2-0.3$ (cross); $0.3-0.4$ (right triangle); $0.4-0.5$ (square); $0.5-0.6$ (star); $0.6-0.7$ (up triangle); $0.7-0.8$ (left triangle); $0.8-0.9$ (plus); $0.9-1.0$ (circle). For sake of clarity we plot values skipped about every 900 time iterations, note that the computational time increment is not constant.

has to be attributed to the low level of turbulence in the top region of the domain; specifically a particle traveling in the top region of the domain (say above $25\delta_S$) tends to remain at the same height or, if trapped in a turbulent structure, it is transported within the near-wall turbulent region. Finally, Fig.4.5 also shows that the slope of the mean vertical displacement decreases in the second half cycle, as particles spread over a large distance and experience the features of turbulence averaged on a larger slab of fluid.

The dispersion along the three directions of the slabs of particles above discussed is shown in Fig.4.6(a). In this section, the dispersion along the i-direction is defined as:

$$x_i^2(t) = \frac{1}{N_p}\sum_{j=1}^{N_p}\left[x_{i,j}(t) - \int_0^t \overline{u_i}(t)dt - x_{i,j}(t=0)\right]^2 \tag{4.1}$$

where N_p is the number of particles belonging to a slab in the fluid column and $x_{i,j}(t)$ is the i-component of the position of the j-particle of the swarm at time t. The dispersion is here related to the fluctuating field only, since the mean displacement given by the averaged velocity field $\overline{u_i}$ ($\int_0^t \overline{u_i}(t)dt$) has been removed. The quantity $\overline{u_i}$ is evaluated at each time step considering the mean velocity of the Lagrangian particles at the position of the j-particle.

Consistently with the classical theory [47], the dispersion in the three directions always increases in time and is characterized by an initial ballistic regime ($t \to 0$) where $x_i^2(t) \sim t^2$ and a Brownian regime ($t \to \infty$) where

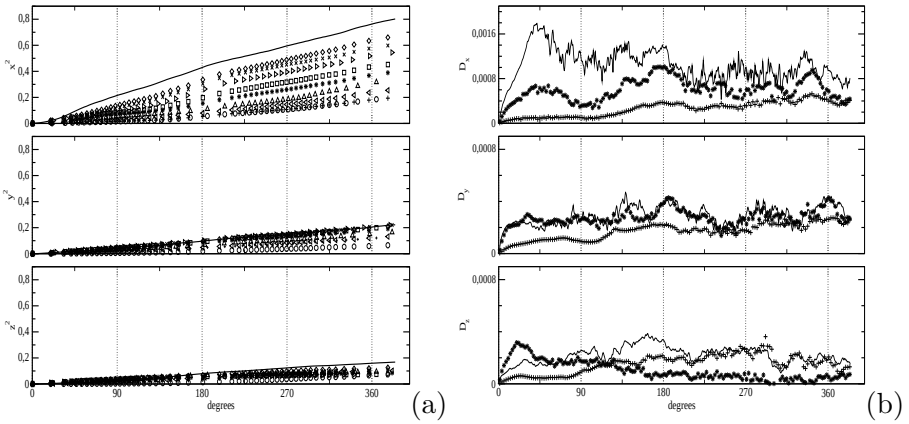

Figure 4.6: a) Dispersion along the three directions for particles released at different heights for the OF (see caption of Fig.4.5 for details); b) diffusivity along the three directions for particles released at different heights for the OF case: $0.0 - 0.1$ (solid line); $0.5 - 0.6$ (star); $0.8 - 0.9$ (plus).

the dispersion increases as t. Our simulations show that the results of the theory hold also in case of wall bounded, inhomogeneous turbulence.

The dispersion along the streamwise direction is much larger than that along the other two directions. Indeed, it is mainly driven by the streamwise velocity fluctuations, whose *rms* value is about three times larger than that relative to the remaining directions, at least in the near-wall region (see [45]). This indicates that the cloud of particles tends to spread in the streamwise direction at a much larger extent than in the other ones. Fig.4.6(a) also shows that the dispersion decreases as the height of release increases.
Due to the low level of turbulence present in the free surface region, the dispersion associated to particles initially released in this region is negligible. Interestingly, we do not observe significant slope change of the dispersion during the phases of velocity inversion, where the level of K is around its own minimum. This is due to the above mentioned effect of large-scale residual turbulence present in the fluid column at the phases of flow reversal.

As a final step, we calculated the diffusivity along each direction as in [48]:

$$D_i(t) = \frac{1}{2}\frac{d}{dt}x_i^2(t) \tag{4.2}$$

where $x_i^2(t)$ is evaluated in Eq.4.1. In Fig. 4.6(b) we show for clarity the diffusivity of three meaningful slabs of particles: near the wall, in the core fluid column and near the free surface region. We observe that the diffusivity obeys the Taylor's two-regime rule ($D_i(t) \sim t$ in the ballistic regime and $D_i(t) \sim$ const in the Brownian one) only for particles released in the turbulent region of the fluid column. The diffusivity is larger for particles initially located in the near-wall region and exhibits anisotropic characteristics

because the streamwise velocity component dominates over the cross-stream ones. Finally, Fig.4.6(b) shows that, for particles initially released within the turbulent layer, particle diffusivity tends to be less sensitive to the initial location during the second half of oscillation owing to the homogenization process above mentioned.

4.3 Particle dispersion in the rotating oscillating flow field

Although rotation does not vary the amount of energy of a system, it can redistribute energy from mean to turbulent flow and *vice versa*. If we consider the viscous length scales δ_S and δ_E previously defined and respectively associated to the oscillatory and the rotational components of the motion, we obtain $\delta_E/\delta_S = \sqrt{Ro}$, in agreement with Eq.1.3 discussed in Sec.1.3. Since our simulations are carried out at $Ro = 1.36$, we expect that rotation increases the thickness of the layer in the water column where turbulent activity is present.
The results of the simulations in the work of Salon et al. [41] show that the specific volume-integrated turbulent kinetic energy increases with respect to the OF case through the increase of the vertical and spanwise components (w and v velocity *rms*) in the fluid column, especially in the half-column near the surface. The presence of the Coriolis force gives rise to a spanwise pressure gradient that oscillates accordingly with the tidal motion. As a result, the mean trajectories of particles follow elliptic paths, and the ratio between the axes varies with the distance from the wall.

Fig.4.7(a) shows the trajectory of four particles originally placed at δ_S. In comparison with OF case of Fig.4.4(a), particles released at the distance of δ_S from the wall are now more broadly dispersed in both vertical (for the presence of a higher turbulence level during the cycle) and horizontal direction (for the presence of the Coriolis term). In the case of particles originally released at $30\delta_S$, far from the boundary layer, the larger turbulent structures are still dominating as in the OF case and trajectories do not exhibit the presence of meaningful vertical mixing except at the end of the cycle.

Fig.4.8(a) shows the mean vertical displacement of the slabs of particles in the OFR case. The rate of increase of the mean vertical displacement is faster than that relative to the OF case in the first quarter of the oscillation cycle, and the largest displacement is observed for the tracers released in the top half column. As shown in [41], this is related to higher vertical velocity fluctuations between 0^o and 90^o along the whole water column, and to an increased level of turbulence in the region closer to the free surface. In the OFR case, the vertical mixing is therefore able to move the tracers released close to the free surface region downward to almost half channel,

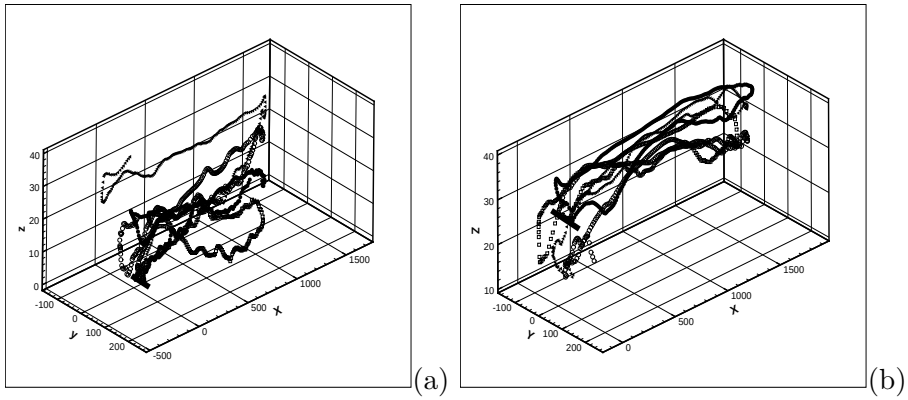

(a) (b)

Figure 4.7: Trajectories of particles along an oscillatory cycle, released at a fixed horizontal station (plotted as a thick segment) at two different heights in the fluid columns: a) $z = \delta_S$; b) $z = 30\delta_S$. For sake of clarity, the ratio among axis is exaggerated and the ticks are in δ_S units.

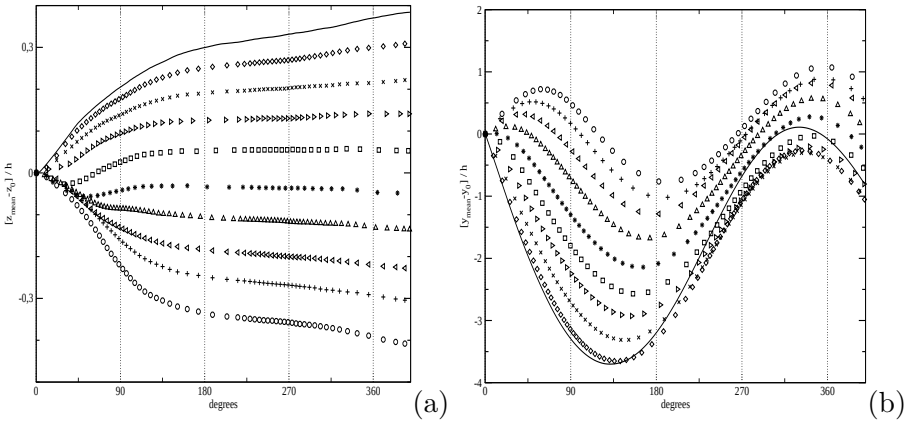

(a) (b)

Figure 4.8: Mean non dimensional vertical (a) and spanwise (b) displacement of tracers released at different heights from the wall for the OFR case (see caption of Fig.4.5 for details).

much more than in the OF case. As an example, in the OFR case the tracers released in the slab between 0.9 and 1.0 of Fig.4.8(a) reach, after a complete oscillation cycle, a mean distance that is more than twice that reached in the OF case (Fig.4.5). Similarly to the OF case, the slopes of the mean vertical displacement decrease in the second half cycle due to the homogenization process above mentioned.
The presence of the cross-stream pressure gradient in the OFR case gives rise to a large spread of tracers in the spanwise direction (Fig.4.8(b)). The maximum mean spanwise displacement is observed in the near-wall region, associated to the largest values of the spanwise velocity component. The mean spanwise displacement decreases and eventually changes its sign going up along the fluid column. This is associated to the shape of the mean profile of the spanwise velocity [41] that, due to the coupling between oscillating and rotating motions, in the first phases of oscillation has negative values in the bottom region and gets positive in the free surface region.

In Fig.4.9 is reported the evolution in the vertical direction of the concentration for particles originally released up to $2\delta_S$ from the bottom (a) and up to $2\delta_S$ from the free surface (b). The concentration is expressed as a ratio with the particles considered N and all the particles $N_{tot} = 102,400$ of the simulation. Particles initially released near the wall are more broadly dispersed in the vertical direction than those released in the upper region. This is due to the presence of an higher level of turbulence at the bottom during the cycle when compared to the free surface [41].

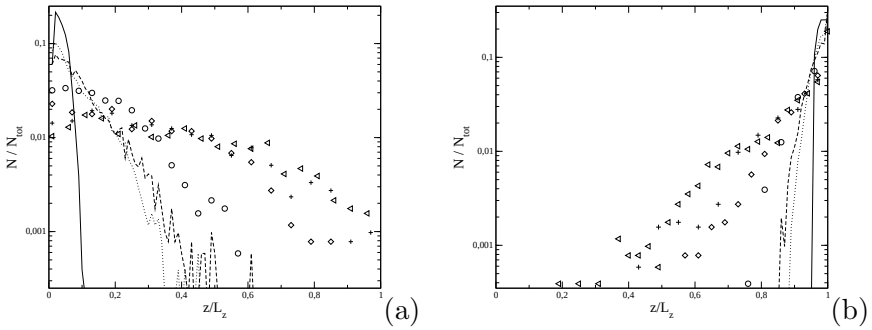

Figure 4.9: The evolution of particle concentration in logarithmic scale along the period simulated in OFR case is showed: on (a) particles originally placed close to the bottom, on (b) particles originally placed close to the free surface. Straight line is the concentration at 1°, dotted line at 15°, dashed line at 30°, circle at 90°, diamond at 180°, plus at 270° and left triangle at 360°.

The dispersion $x_i^2(t)$ along the three directions of the tracers released in the slabs is computed as in Eq.4.1, and shown in Fig.4.10(a).
The streamwise velocity *rms* is slightly affected by rotation in the near-

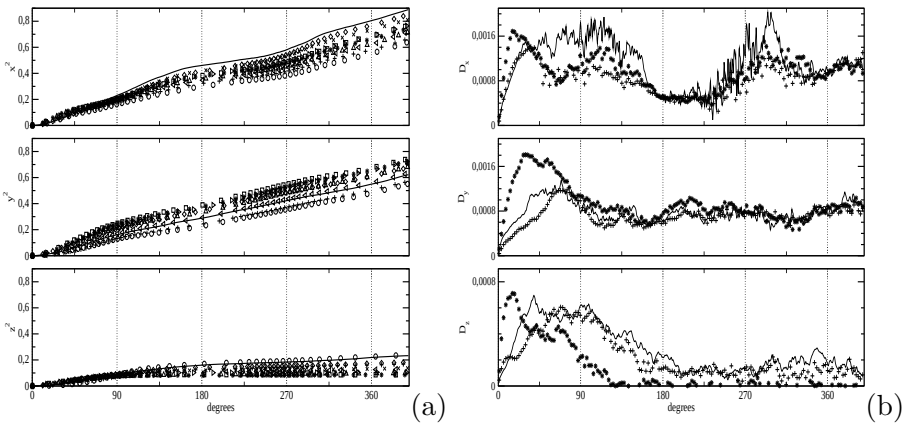

Figure 4.10: a) Dispersion along the three directions for particles released at different heights for the OFR case (see caption of Fig.4.5 for details); b) diffusivity along the three directions for particles released at different heights for the OFR case (see caption of Fig.4.6b for details).

wall region, whereas it increases in the free-surface region; as a result, the streamwise dispersion related to particles released close to the free surface is much more affected by rotation than the near-bottom ones. A similar behavior is observed for the vertical dispersion, because the quantity w_{rms} is strongly enhanced by rotation in the core region as well as in the free-surface region. Therefore, particles released in the upper part of the fluid column show a vertical dispersion larger than that relative to the non-rotating case (compare the third plot of Fig.4.10(a) with that of Fig.4.6(a).

The most relevant difference between OF and OFR is observed in the dispersion along the spanwise direction: in the OFR case, after one cycle of oscillation, due to the higher spanwise velocity *rms* and to the non-zero Reynolds shear stresses τ_{12} and τ_{23}, y^2 has values comparable with x^2, with the tracers released in the core region characterized by the largest dispersion. The turbulent mixing is therefore more efficient in the OFR case: in particular, rotation enhances the dispersion in the horizontal planes and, at the same time, thickens the fluid layer where a large spreading of the particulate is observed.

Fig.4.10(b) shows that the diffusivity along the streamwise direction behaves quite differently in the first and in the second half cycle of oscillation. For particles released in the near-wall region, after a sudden increase similar to the OF case, D_x reaches nearly constant values, comparable with those of the OF case. Conversely, the streamwise diffusivity of tracers released in the core and in particular in the near-surface regions is larger than in the OF case, due to the already discussed increase of turbulence level in the free surface region. As in the previous case, in the second half cycle D_x looses the memory of the tracers initial location, consistently with the homoge-

nization process. The second half cycle is also characterized by a strong increase in streamwise diffusivity with respect to the OF case, especially for tracers released in the core and the near-surface regions, coherently with the increased slope of the dispersion and with the above mentioned asymmetry in the turbulence dynamics.
In the first half cycle, the vertical diffusivity is larger than that of the OF case, especially for tracers released in the core region. This is due to the augmented level of turbulent mixing in such region, that is basically related to the higher vertical velocity *rms* and to the non-zero correlation between vertical and spanwise velocity fluctuations. In the second half cycle D_z homogenizes and decreases to values comparable to those of the OF case.
As observed for dispersion, the amplitude of the diffusivity in the spanwise component results comparable to the streamwise one. After 90^o, D_y appears nearly constant along the whole column, justifying the efficiency of the horizontal mixing.

A final comparison between case OF and OFR is showed in Fig.4.11. On each panel (left side is OF case and right OFR) is sketched the instantaneous position of particles originally contained in different slabs: in this case, we divided in three equal parts the water column, from the bottom to $13\delta_S$, from 13 to $26\delta_S$ and from $26\delta_S$ up. Particles positions are showed during their evolution at four instants along the cycle simulated. Axis are made non-dimensional with the column depth h and furthermore the vertical dimension is exaggerated to evidence the vertical mixing of particles. In OFR case (all the right panels), due to the presence of an higher level of turbulence and of the Coriolis force, particles are more broadly dispersed both in vertical and in horizontal direction than in OF case (all the left panels); particles originally released close to the bottom (both in OF and OFR case) are subjected to an higher level of turbulence than those originally placed close to the free surface and therefore can be involved in the turbulent mixing and reach higher levels of the column.

In order to visualize the mixing properties of the Eulerian flows herein discussed, we attach a CD with the animations of the dispersed phase in both OF and OFR case.

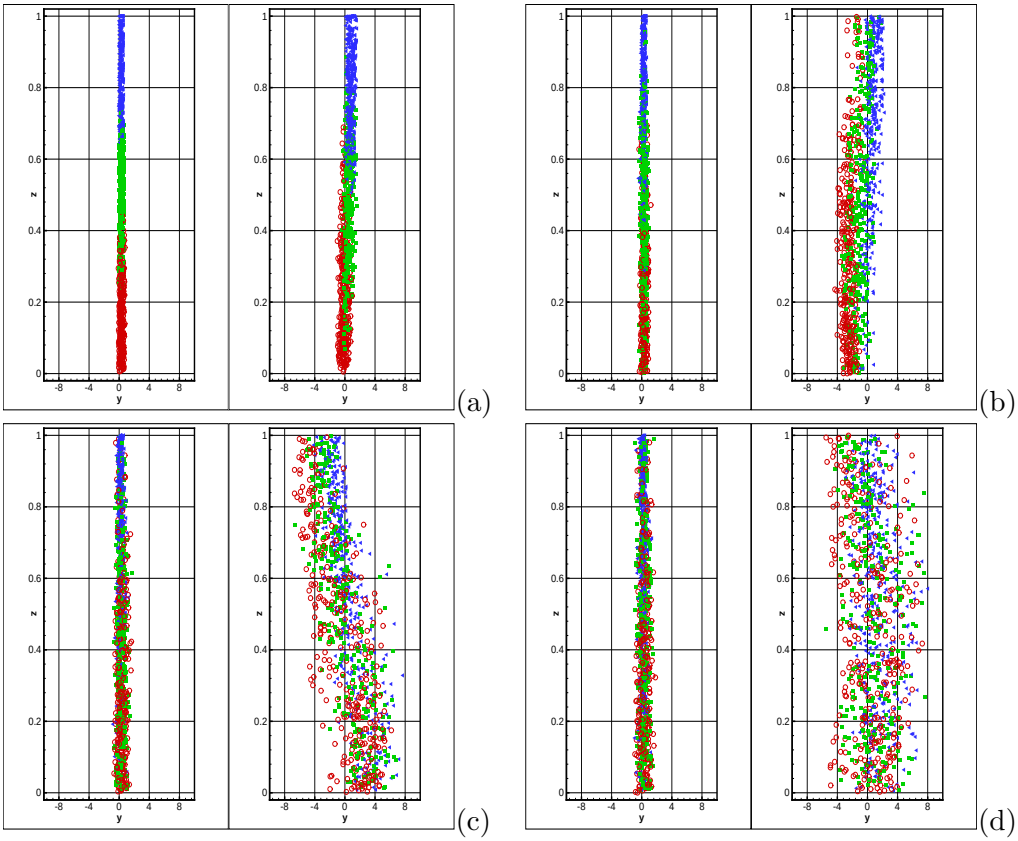

Figure 4.11: On (a) 15°, on (b) 90°, on (c) 270°, on (d) 360°. All the left panels are relative to the OF case and all the right panels are relative to OFR case. Red circles indicates particles released at the bottom of the fluid column; green square at the core and blue triangles at the top.

Chapter 5

Conclusion

5.1 Concluding remarks

The specific target of this work is the description of the mixing properties of a tidally driven water column. In particular, the dispersion of fluid particles, representative of a shallow-water marine environment, has been investigated. We performed a small-scale numerical experiment employing physical parameters relative to the Gulf of Trieste, thus considering a tidally-driven, mid-latitude case. A large number of particles has been released in the flow field under two different conditions: first the dispersion of the particulate in the purely oscillatory flow was studied; subsequently the dispersion in the oscillating-rotating case was investigated.

As regards the response of particles in the turbulent Stokes boundary layer (OF case), we observed the presence of two distinct regions in the water column, namely a near-wall one characterized by small-scale turbulent structures and a free surface region where turbulent mixing is very weak.
Moreover, we observed that dispersion and diffusivity obey the two classical regimes as theorized by Taylor, respectively the ballistic and the Brownian regimes. The streamwise component of the dispersion dominates over the other two, and tracers result essentially dispersed along the mean flow direction. In particular, particles released near the wall are more broadly dispersed than those released in the upper region.
During the flow reversal, although the level of turbulent fluctuations rapidly decays, particle dispersion is mainly governed by the presence of weak, large-scale structures remaining in the fluid column as an history effect from the previous phases of the cycle.

In the OFR case herein investigated, rotation has two main effects on the flow field: 1) it causes an increase of the horizontal and the vertical turbulent mixing; 2) it thickens the turbulent depth in the fluid column.
As a result, both in the core region and in the free surface region the particulate is dispersed at a much larger extent than in the OF case. The

presence of a mean spanwise velocity raised by the Coriolis force severely affects the dispersion in the spanwise direction within the whole fluid column. The tracers diffuse mainly on horizontal planes, with intensities that are similar in both the streamwise and the spanwise components.
The results of the present work do interest a mid-latitude shallow-water problem. Although it is possible to argue that rotation enhances spanwise dispersion of the particulate, more research is eventually needed in order to evaluate particle dynamics dependence on different values of the Rossby number.

Bibliography

[1] F. Stravisi *Caratteristiche oceanografiche del Golfo di Trieste.* Parco Marino di Miramare, Hydrores, 6, 39-45 (1988).

[2] F. Stravisi *The IT method for the harmonic tidal prediction.* Boll. Oceanol. Teor. Appl., 1, 3, 193-204 (1983).

[3] Y. Noh, H.S. Min and S. Raasch *Large eddy simulation of the ocean mixed layer: the effects of wave breaking and Langmuir circulation.* J. of Phys. Oceanography, Volume 34, April (2004).

[4] G.D. Craig and M.L. Banner *Modeling wave enhanced turbulence in the ocean surface layer.* J. Phys. Oceanogr. 24, 2546-2559 (1994).

[5] J.C. McWilliams and C.H. Moeng *Langmuir turbulence in the ocean.* J. Fluid Mech., 334:1-30 (1997).

[6] F. Stravisi *Winter dense water formation in the Gulf of Trieste.* Rep. Meteor. Oceanogr., Harvard Un. 40, I, 291-293 (1992).

[7] F. Stravisi *La temperatura del mare a Trieste (1946-1999).* Hydrores, 20, 7-16 (2000).

[8] S. Komori, H. Ueda, F. Ogino and T. Mizushina *Turbulent strucutre in a stably stratified open channel flow.* J. Fluid Mech., 130, 13 (1983).

[9] V. Armenio and S. Sarkar *An investigation of stably stratified turbulent channel flow using Large Eddy Simulation.* J. Fluid Mech., 459, 1 (2002).

[10] V. Malačič *Thermohaline Anomalies in the Spring and Early Summer of 2000 in the Gulf of Trieste.* Oceanol. Acta 14, 23-32 (1991).

[11] G. Comini *Fondamenti di termofluidodinamica computazionale.* SGE Editoriali Padova (2004).

[12] M. R. Maxey and J. Riley *Equation of motion for a small rigid sphere in a nonuniform flow.* Phys. Fluids 26, 883 (1983).

[13] C. Crowe, M. Sommerfeld and Y. Tsuji *Multiphase flows with droplets and particles.* CRC Press (1998).

[14] V. Armenio and V. Fiorotto *The importance of the forces acting in particles in turbulent flows.* Phys. Fluids 13, 8 (2001).

[15] M. Germano, U. Piomelli, P. Moin and W. H. Cabott *A dynamic subgrid-scale eddy viscosity model.* Phys. Fluids A 3, 1760-1765 (1991).

[16] V. Armenio and U. Piomelli *A Lagrangian Mixed subgrid-scale model in generalized coordinates.* Flow, Turbulence and Combustion 65, 51-81 (2000).

[17] U. Piomelli *Large eddy and direct simulation of turbulent flows.* Class notes, pag. 31 (2004).

[18] J. Bardina, J. H. Ferziger and W. C. Reynolds *Improved subgrid scale models for Large Eddy Simulation.* AIAA Paper No. 80-1357 (1980).

[19] Y. Zang, R.L. Street and J.R. Koseff *A non staggered grid fractionale step method for time-dependent incompressible Navier-Stokes equations in curvilinear coordinates.* J. Comput. Phys. 114, 18-33 (1994).

[20] C.A.J. Fletcher *Computational Techniques for Fluid Dynamics. Volume II.* Springer-Verlang (1988).

[21] C.A.J. Fletcher *Computational Techinques for Fluid Dynamics. Volume I.* Springer-Verlang (1988).

[22] J.H. Ferziger and M. Peric *Computational Methods for Fluid Dynamics.* Springer-Verlang (2000).

[23] Y. Aoyama *Practical MPI programming* International Technical Support Organization, IBM (1999).

[24] S. Salon, V. Armenio and A. Crise *Parallelization of a code for Large Eddy Simulation.* Science and Supercomputing at Cineca, Es286 (2003).

[25] Consorzio Interuniversitario at Casalecchio di Reno, Bologna (Italy) *http://www.cineca.it.*

[26] Q. Zou and M. A. Leschziner *An improved particle-locating algorithm for Eulerian-Lagrangian computations of two-phase flows in general coordinates.* International Journal of Multiphase Flow 25, 813-825 (1999).

[27] P.K. Yeung and S.B. Pope *An algorithm for tracking fluid particles in numerical simulations of homogeneus turbulence.* J. Comput. Phys. 83, 96-125 (1989).

[28] K. Kontomaris, T.J. Hanratty and J.B. McLaughlin *An algorithm for tracking fluid particles in a spectral simulation of turbulent channel flow.* J. Comput. Phys. 103, 231-242 (1992).

[29] P.J. Oliveira, A.D. Gosman and R.I. Issa *A method for particle location and field interpolation on complex, three-dimensional computational meshes.* J. Adv. Engng. Software, 28, 607-614 (1997).

[30] C. Marchioli, V. Armenio and A. Soldati *Simple and accurate scheme for fluid velocity interpolation for Eulerian-Lagrangian computation of dispersed flows in 3-D curvilinear grids.* In printing on J. Comput. Phys. (2007).

[31] F.K. Chow and R.L. Street *Explicit filtering and reconstruction turbulence modelling for Large Eddy Simulations of field-scale flows.* Advances in Hydro-Science and Engineering, volume VI (2000).

[32] S. Stolz, N. Adams and L. Kleiser *An approximate deconvolution model for LES with applications to incompressible wall-bounded flows.* Phys. Fluids 13, 4 (2001).

[33] J.G.M. Kuerten *Subgrid modeling in particle-laden channel flow.* Phys. Fluids 18, 2 025108 (2006).

[34] E. Weisstein *http://mathworld.wolfram.com/Deconvolution.html.* Wolfram Research.

[35] B. Shotorban and F. Mashatek *Modeling subgrid scale effects on particles by approximate deconvolution.* Personal comunication (2005).

[36] G. Lupieri and V. Armenio *An MPI code for Lagrangian dispersion in a turbulent Eulerian field.* Science and Supercomputing at Cineca, 378-382 (2005).

[37] Benchmark simulation on channel flow *http://www-mvt.iw.unihalle.de/workshop05/workshop05.html.*

[38] J.G.M. Kuerten *Can turbophoresis be predicted by Large eddy Simulation?* Phys. Fluids 17, 011701 (2005).

[39] S. Salon *Turbulent mixing in the Gulf of Trieste under critical conditions.* Ph. D. Thesis (2004).

[40] T. Sarpkaya *Coherent structures in oscillatory boundary layers.* J. Fluid Mech. 253, 105 (1993).

[41] S. Salon, V. Armenio and A. Crise *Large-eddy simulation of an oscillating-rotating turbulent flow.* In: Humphrey JAC, Gatski TB, Eaton JK, Friedrich R, Kasagi N, Leschziner MA (eds) Proc. Turbulent and Shear Flow Phenomena 4, Vol.1. (2005).

[42] B.L. Jensen , B.M. Sumer and J. Fredsøe *Turbulent oscillatory boundary layers at high Reynolds numbers.* J. Fluid Mech., 56, 533 (2002).

[43] D.J. Tritton *Physical fluid dynamics.* Oxford University Press Inc. New York (1998).

[44] G.N. Coleman, J.H. Ferziger and P.R. Spalart *A numerical study of the turbulent Ekman layer.* J. Fluid Mech., 213, 313 (1990).

[45] S. Salon, V. Armenio and A. Crise *A numerical investigation of the Stokes boundary layer in the turbulent regime.* J. Fluid Mech. 570, (2007).

[46] M. Hino, M. Kashiwayanagi, A. Nakayama and T. Hara *Experiments on the turbulent statistics and the structure of a reciprocating oscillatory flow.* J. Fluid Mech. 131, 363-400 (1983).

[47] G. Taylor *Diffusion by continuous movements.* Proc. Lond. Math. Soc. 20, 196-212 (1921).

[48] S. Elghobashi and G.C. Truesdell *On predicting particle-laden turbulent flows.* J. Fluid Mech. 242, 655-700 (1992).

Acknowledgements

The author wishes to thank Prof. V. Armenio and Ph.D. S. Salon for their help and patience.
Thanks to my family for the support expressed in these years.